

# SPECTROSCOPIC COMPARISON OF METAL-RICH RRAB STARS OF THE GALACTIC FIELD WITH THEIR METAL-POOR COUNTERPARTS

MERIEME CHADID<sup>1</sup>, CHRISTOPHER SNEDEN<sup>2</sup>, AND GEORGE W. PRESTON<sup>3</sup>,

<sup>1</sup>Université Nice Sophia–Antipolis, Observatoire de la Côte d’Azur, UMR 7293, Parc Valrose, F-06108, Nice Cedex 02, France; chadid@unice.fr

<sup>2</sup>Department of Astronomy and McDonald Observatory, The University of Texas, Austin, TX 78712, USA; chris@verdi.as.utexas.edu

<sup>3</sup>Carnegie Observatories, 813 Santa Barbara Street, Pasadena, CA 91101, USA; gwp@obs.carnegiescience.edu

## ABSTRACT

We investigate atmospheric properties of 35 stable RRab stars that possess the full ranges of period, light amplitude, and metal abundance found in Galactic RR Lyrae stars. Our results are derived from several thousand echelle spectra obtained over several years with the du Pont telescope of Las Campanas Observatory. Radial velocities of metal lines and the H $\alpha$  line were used to construct curves of radial velocity *versus* pulsation phase. From these we estimated radial velocity amplitudes for metal lines (formed near the photosphere) and H $\alpha$  Doppler cores (formed at small optical depths). We also measured H $\alpha$  emission fluxes when they appear during primary light rises. Spectra shifted to rest wavelengths, binned into small phase intervals, and coadded were used to perform model atmospheric and abundance analyses. The derived metallicities and those of some previous spectroscopic surveys were combined to produce a new calibration of the Layden abundance scale. We then divided our RRab sample into metal-rich (disk) and metal-poor (halo) groups at [Fe/H] =  $-1.0$ . The atmospheres of RRab families, so defined, differ with respect to (a) peak strength of H $\alpha$  emission flux, (b) H $\alpha$  radial velocity amplitude, (c) dynamical gravity, (d) stellar radius variation, (e) secondary acceleration during the photometric bump that precedes minimum light, and (g) duration of H $\alpha$  line-doubling. We also detected H $\alpha$  line-doubling during the “bump” in the metal-poor family, but not in the metal-rich one. Though all RRab probably are core helium-burning horizontal branch stars, the metal-rich group appear to be a species sui generis.

*Keywords:* hydrodynamics methods: observational stars: atmospheres stars: oscillations stars: variables: general techniques: spectroscopic

## 1. INTRODUCTION

Because of their moderately high luminosities,  $M_V \sim 0.5$  (Arp 1959) and plentiful numbers in globular clusters (hereafter GC) and in the Galactic field, much effort has been expended to calibrate the RR Lyrae stars as standard candles, both observationally, e.g., Kollmeier et al. (2013) and theoretically, e.g. Marconi et al. (2015) in order to explore the spatial and kinematic structures of the Galactic halo and its attendant satellite systems. Bailey’s (1902) subtypes RRa and RRb exhibit periodic pulsations ( $0.4 < P < 0.9$  d) in the fundamental mode with strongly skewed light variations of large amplitude ( $\sim 1$  visual magnitude) that are readily detected by conventional photometric methods.

The RRab stars of the Galactic field possess a large range in metallicity (Preston 1959; Layden 1994), including a metal-rich component with disk spatial distribution and kinematic properties (Preston 1959; Layden 1995a,b) that has no counterpart among the Galactic GCs. Metallicities as high as solar ([Fe/H] = 0)<sup>1</sup> occur and the fundamental periods are systematically smaller than those of more metal-poor variables. In particular the Galactic field contains metal-rich RRab stars with large light amplitudes,  $\Delta V > 1$ , and periods less than 0.43 d that have never been found in any GC. RRab stars with these characteristics are more concentrated toward the Galactic plane than RRab stars of longer period. This metal-rich short-period extension in the Galactic field is historically the first metallicity effect encountered in the RRab family. Kukarkin (1949) first called attention to this anomaly more than 65 years ago. How the metal-rich RRab stars should be apportioned between the thick disk (Gilmore & Reid 1983) and an old thin disk

<sup>1</sup> We adopt the standard spectroscopic notation (Wallerstein & Helfer 1959) that for elements A and B,  $[A/B] \equiv \log_{10}(N_A/N_B)_\star - \log_{10}(N_A/N_B)_\odot$ . We use the definition  $\log \epsilon(A) \equiv \log_{10}(N_A/N_H) + 12.0$ , and equate metallicity with the stellar [Fe/H] value.

(Preston et al. 1991, Layden 1994, Morrison et al. 1990) has yet to be determined.

In Figure 1, adapted from Figure 1 of Layden (1995b) we present a plot of pulsation period *versus*  $[\text{Fe}/\text{H}]$  for the RRab stars tabulated by (Layden 1994, hereafter called Lay94). Periods were taken from the General Catalog of Variable Stars (GCVS; Samus et al. 2010<sup>2</sup>, except for metal-rich CI And for which we used the period derived by (Schmidt 1991). We adopt a division between metal-poor (blue circles) and metal-rich (red circles) stars at  $[\text{Fe}/\text{H}] = -1.0$  in view of the abrupt changes in kinematic properties at this metallicity assembled in Layden’s (1995a) Figures 1, 3, and 4. We are mindful of the *bonafide* overlap of the abundance distributions of the Galactic halo and disk (Morrison et al. 1990, Ruchti et al. 2011). Regrettably, the small data sample of the present investigation is not well-suited to investigate such overlap in the RRab populations.

The trend in Figure 1 toward shorter periods with increasing  $[\text{Fe}/\text{H}]$  is accompanied by a modest decrease in luminosity ( $\sim 1$  magnitude) that has been the subject of numerous investigations summarized by McNamara (1999). Conclusions about the nature of the metal rich component are insensitive to the precise location of the disk-halo abundance division point at the 0.1 dex level. Zinn (1985) placed the boundary between disk and halo GCs at  $[\text{Fe}/\text{H}] = -0.8$ ; a choice that would not materially affect the present study.

The great majority of Zinn’s (1985) disk GC have red horizontal branches that contain few, if any, RRab variables. The one RRab star in the metal-rich globular cluster 47 Tuc has a long period of 0.737 d (Carney et al. 1993). Contrary to all expectations Rich et al. (1997) reported that two metal-rich GCs, NGC 6388 and NGC 6441, possess extended blue HBs, and subsequent searches for variable stars (Pritzl et al. 2002, Corwin et al. 2006) revealed the presence of numerous RRab stars with unexpectedly long periods. The period distributions of the metal rich field and cluster variables barely overlap, as is evident from a glance at Figure 1. Clearly, the metal-rich RRab stars of the Galactic field and those in Zinn’s disk GCs are not drawn from the same parent population, an anomaly recognized already by Layden (1995b). The reason for the different period distributions of the field and GC metal-rich RRab populations is unknown at present. We suppose that a complete explanation will address the existence of multiple stellar populations in these two GCs (Bellini et al. 2013) and will appeal to model calculations of the sort made by Bono et al. (1997a,b) and Marconi et al. (2015). An early, semi-empirical explanation of metal-rich RRab stars by Taam et al. (1976) required a special HB evolutionary scenario, preceded by very large ( $\sim 0.5M_{\odot}$ ), unverified mass loss during RGB evolution. Though never discredited, their proposal is not widely accepted, and the search for antecedents of metal-rich RRab stars continues.

Although a multitude of fascinating photometric characteristics of the RR Lyrae stars have been investigated intensively in recent times, with particular emphasis on the mysterious Blazhko (1907) phenomenon, the relatively few high-resolution spectroscopic surveys have been directed primarily toward derivation of elemental abundances and toward luminosities via the Baade-Wesselink method. We recognize the interest that attends the Blazhko mystery. However, from the perspective of this paper the Blazhko phenomenon only complicates an already overburdened topic. We limit our discussion to stable RRab stars as defined by Chadid & Preston (2013), deferring Blazhko issues to a subsequent investigation.

This paper is devoted to a detailed high-resolution spectroscopic comparison of samples of nearby metal-rich and metal-poor RRab stars of the Galactic field that have been observed at Las Campanas Observatory during the past decade (see Preston 2011 §5.1). We derive stellar atmospheric parameters effective temperature, microturbulent velocity, and gravity as functions of pulsation phase,  $[\text{Fe}/\text{H}]$  metallicity, and period. Radial velocities, derived separately from metal lines and from the  $\text{H}\alpha$  line of hydrogen, are used to explore changes in the atmospheric structures of these stars that occur during their pulsation cycles. We place extant metallicity results from several surveys on a common system, and derive relative abundance ratios of several elements. Then we compare the kinematic behaviors of metal-rich and metal-poor RRab envelopes. We find significant differences between the envelope kinematics of RRab abundance families, *families that are defined solely by their Galactic kinematics* (Layden’s 1995a Figures 1, 3, and 4). This surprises us. Insofar as we are aware these differences play no role in either the construction or interpretation of horizontal branch models. They are phenomena sui generis.

## 2. OBSERVATIONS AND REDUCTIONS

The survey of RRab stars upon which this paper rests was conducted with the echelle spectrograph of the du Pont telescope. The spectrograph was configured in the manner used for our previous RRab and RRc metallicity studies (For et al. 2011a,b; Govea et al. 2014). Specifically, the instrument was used with a 1.5 x 4.0 arcsec aperture which

<sup>2</sup> <http://www.sai.msu.su/gcvs/gcvs/>

yielded a resolving power  $R = \lambda/\Delta\lambda \sim 27000$  at  $5000 \text{ \AA}$  and wavelength coverage  $\lambda\lambda 3400\text{--}9000$ .

Observations were gathered in the eight-year interval 2006–2013. In 2006–2009 ten RRab stars with periods near 0.57 d were observed to provide a basis for comparison of s-process rich TY Gru (Preston et al. 2006) with RRab stars of normal halo composition. Following discovery in 2009 of emission and absorption lines of He I and He II in AS Vir the survey was extended to 24 additional stars that sample the entire ranges of period, light amplitude, and metallicity encountered in the RRab family (Preston 2009, 2011). These additional stars, listed in Table 1, were observed intensively during twenty 5- to 7-night runs during the years 2009–2013.

The photometric periods of our program stars range from 0.39 to 0.71 days, during which they vary in brightness with light amplitudes on  $0.63 < V_{amp} < 1.28$  and highly correlated metal radial velocity amplitudes,  $50 < \Delta RV < 70 \text{ km s}^{-1}$  (Table 1). We limited our exposure times to a maximum of 600 s. More typically the exposures were 400 s, with some as short as 200 s. The maximum integration times were thus less than 2% of the shortest pulsation period among our program stars. This procedure rendered the  $RV$  variations that occur during integrations much smaller than other spectral line broadening effects in individual observations. However, the integration-time restriction resulted in low signal-to-noise individual spectra.

Note that particular emphasis was placed on primary light rises due to initial interest in the shock phenomena that produce hydrogen and helium emission. We have come to regret this tactic, because it led to inadequate phase coverage of phenomena during declining light that we only became aware of late in the survey.

We extracted spectra from the original CCD image files using procedures discussed previously (Preston & Sneden 2000; For et al. 2011a); for the most part the description of these reduction steps need not be repeated here. However, we have adopted one shortcut in the removal of scattered light from our spectra that deserves discussion inasmuch as it bears on the accuracy of abundances derived in this paper and their use in recalibration of the RR Lyrae abundance scale.

### 2.1. Removal of Scattered Light from du Pont echelle spectra

For et al. (2011b) describe a scattered light problem peculiar to the du Pont echelle spectrograph, and they outline a procedure used to remove scattered light from their observations. This special technique is required because the projected length of the entrance aperture of the du Pont echelle, constrained by prismatic order separation, is too small longward of  $5000 \text{ \AA}$  to permit subtraction of scattered light by use of pixels adjacent to the projected stellar image. In this paper we use a greatly simplified procedure, namely, subtraction of a constant fraction of the stellar flux at each pixel along each echelle order. This model attributes all scattered light to small-angle scattering into regions immediately adjacent to each spectral order. It ignores large-angle scattering that could, for example, flood high (blue-violet) orders with red light from distant low (red) spectral orders in the echelle format. Large-angle scattering into blue-violet orders can be important in the case of cool, red stars, but RR Lyrae are not very red, so our simplified correction works well. We demonstrate this with measurements of equivalent widths ( $EW$ ) in the spectrum of one of our radial velocity standard stars, the metal-poor subgiant HD 140283. This star is somewhat redder ( $B - V = 0.50$ ) than the RRab stars, for which colors lie in the range  $0.1 < B - V < 0.5$  during their pulsation cycles.

We added 38 du Pont echelle spectra of HD 140283, flattened them, subtracted 0.1 from the normalized continua in all orders, and renormalized. The  $S/N$  in this spectrum increases from 250 at  $4000 \text{ \AA}$  to 500 at  $5500 \text{ \AA}$ . For this test we used the IRAF/splot<sup>3</sup> package to measure  $EW$ s of the Fe I and Fe II lines that were measured in a Subaru spectrum of HD 140283 by Gallagher et al. (2010). We correlate these two  $EW$  sets in Figure 2, plotting the Subaru values (labeled EWS) *versus* those from du Pont (EWD) in panel (a), and line-by-line differences  $EWS - EWD$  as functions of line strength EWS in panel (b) and wavelength in panel (c). The agreement is good:  $\langle EWS - EWD \rangle = -0.48 \text{ m\AA}$ , with standard deviation  $\sigma = 1.01 \text{ m\AA}$  from 83 lines in common.

The  $EW$  differences in panel (c) of the figure allow us to investigate whether large angle scattering from the brighter low (red) orders in the du Pont spectrograph produces wavelength-dependent residuals. The lack of significant variation with wavelength leads us to conclude that our scattered light corrections are acceptable, i.e., they play an insignificant role in the error budget of our abundance analyses.

## 3. MODEL ATMOSPHERES AND CHEMICAL COMPOSITIONS

We derived model atmosphere parameters effective temperature  $T_{\text{eff}}$ , surface gravity  $\log g$ , metallicity  $[\text{Fe}/\text{H}]$  and microturbulent velocity  $\xi_t$  for each program star at many pulsational phases, following the procedures discussed by

<sup>3</sup> IRAF is distributed by the National Optical Astronomy Observatory, which is operated by the Association of Universities for Research in Astronomy (AURA) under cooperative agreement with the National Science Foundation.

For et al. (2011b) and Govea et al. (2014). The integration time restrictions outlined in §2 yielded low signal-to-noise spectra, frequently  $S/N < 20$ . To increase S/N we created co-added spectra in the following manner. For each star we sorted all available spectra in order of increasing pulsation phase by use of the elements in Table 1. We divided these sorts into phase bins. The bounds of these phase intervals chosen for co-addition were dictated in most instances by vagaries of the phase distributions. The phase intervals of the bins were generally smaller than 0.05 P and never larger than 0.10 P. The number of spectra per bin ranged from 3 to 10. We excluded observations made on  $0.6 < \phi < 0.9$  because of large macroturbulent velocities that degrade the spectra in this phase interval (Preston & Chadid 2013). Each spectrum in each bin was shifted to rest wavelength with IRAF/dopcor by use of radial velocities measured in IRAF/fxcor. Finally, average spectra were created from these shifted spectra by use of IRAF/scombine.

### 3.1. Model Atmosphere and Abundance Calculations

We used the co-added spectra to first derive their model atmospheric parameters. We also decided to re-derive models and abundances for the 10 stars originally discussed by For et al. (2011b), in order to ensure that their parameters were on the same system that we employed for the rest of our sample. We used spectra of one co-added phase bin at  $\phi = 0.5$  for their stars. Here we highlight the main analytical points and note any substantive differences between the present and previous studies.

We adopted the line list of For et al. (2011b), updating the transition probabilities with new laboratory values for Ti I (Lawler et al. 2013), Ti II (Wood et al. 2013), and Fe I (Den Hartog et al. 2014), combining these with values from O’Brian et al. (1991) for lines with excitation energies  $\chi < 2.3$  eV. For these lines we measured *EW*s using an Interactive Data Language (IDL)<sup>4</sup> code developed by Roederer et al. (2010) and Brugamyer et al. (2011). These line lists and interpolated ATLAS (Kurucz (2011) and references therein) model atmospheres were used as inputs to the current version of the *LTE* line analysis code *MOOG* (Snedden 1973)<sup>5</sup>. In the analyses we eliminated those lines that are too weak for reliable measurement.

The results of these calculations were line-by-line abundances for all species. The parameters of the models were altered and the line analyses repeated to derive: (a)  $T_{\text{eff}}$ , so that there be no average trend of abundances with excitation energy derived from Fe I lines; (b)  $\xi_t$ , so that there be no average trend of abundances from Fe I with *EW*; (c)  $\log g$ , so that mean abundances derived from Fe I and Fe II agree well, and secondarily the mean abundance derived from Ti I not be in severe disagreement with that from Ti II; and (d)  $[M/H]$ , so that the assumed model metallicity was close to the derived  $[Fe/H]$  value. This procedure took typically three or fewer iterations. The rapidity of convergence was a result of two RRab properties. First, within the confines of traditional analyses, the RRab stars occupy a relatively small region of model parameter space, typically  $6000 < T_{\text{eff}} < 7000$  K,  $1.7 < \log g < 2.7$ , and  $2.5 < \xi_t < 3.5$  km s<sup>-1</sup>. Second, these stars are warm enough that the free electrons needed for the dominant H<sup>-</sup> continuous opacity are largely donated from H itself instead of the easily ionized metals, and so the widely-ranging metallicities ( $-2.5 < [M/H] < 0.0$ ) do not severely affect the model atmosphere structures.

We also derived several abundance ratios  $[X/Fe]$  for each program star at each pulsational phase. However, abundance ratios are of secondary interest in this paper, so given the *S/N* limitations of our spectra we have chosen to present in Table 4 mean abundance ratios  $[X/Fe]$  for each star only for species that were available for analysis at most phases of most stars: Ca I, Sc II, Ti I & II, Cr I & II, Mn I, and Ba II, along with the mean  $[Fe/H]$  metallicities. All abundance ratios are referenced to the solar photospheric values recommended in the Asplund et al. (2009) review. Those values are in many cases based on analytical assumptions (e.g., non-LTE, multi-stream modeling) that are beyond the scope of our standard abundance analysis techniques. Recently, a series of papers (Grevesse et al. 2015; Scott et al. 2015a,b) has updated the solar abundances, computing them in a variety of ways. The solar abundance differences they derive are typically not large, usually less than 0.05 dex for the species of interest here. These are small uncertainties compared to the other error sources in our work.

The abundance ratios were computed for the same ionization-state abundances in numerator and denominator, e.g.,  $[Ca/Fe]$  from Ca I and Fe I, and  $[Sc/Fe]$  from Sc II and Fe II. These ratios have been computed from those derived at each phase for a star. At the bottom of this table we also list the mean line-to-line abundance scatters for each species  $\langle \sigma \rangle$  and the mean number of lines employed in the calculations  $\langle n \rangle$  in individual star/phase abundance derivations. These numbers can vary from star to star and phase to phase, but suggest that the  $\sigma$  values never are less than  $\simeq 0.1$ . Additionally, some species are represented by three or fewer transitions. Such abundance results should not be

<sup>4</sup> IDL is proprietary software system distributed by Exelis Visual Information Solutions, Inc., and is available at <http://www.exelisvis.com/ProductsServices/IDL.aspx>.

<sup>5</sup> Available at <http://www.as.utexas.edu/~chris/moog.html>.

over-interpreted.

Final model atmosphere parameters for the program stars in all co-added phase bins are listed in Table 3. In considering these values the reader should keep in mind that they result from application of static, plane-parallel model atmospheres and LTE line analysis techniques to stellar atmospheres that are highly dynamic. In less than a day the RRab stars cycle through correlated variations of 1000 K in  $T_{\text{eff}}$  and 1 dex in  $\log g$  and  $\xi_t$  (e.g., For et al. 2011b). The derived spectroscopic gravities have static and dynamic components. Moreover, the derived microturbulent velocities reflect both the standard small-scale turbulent velocities that are applied in analyses of non-variable stellar atmospheres and radial velocity gradients within the line forming regions of RR Lyrae pulsators.

The derived absolute quantities should be viewed with caution. Relative values from star to star among our RRab sample should be much more reliable. All spectral features studied in this paper are due to “photospheric” absorptions by  $\alpha$ - and Fe-group elements in a restricted strength ( $EW$ ) range. Thus their lines are formed in similar atmospheric layers, and their abundance ratios should be less sensitive to modeling uncertainties than are the individual abundances.

### 3.2. Correlations of Model Parameters with Pulsation Phases and Metallicities

The derived temperatures of our stars vary with phase in a manner broadly consistent with the results of For et al. (2011a). Immediately after maximum light the temperatures decline, rapidly at first and then more slowly from phase  $\sim 0.3$  to phase 0.6, the upper phase limit of our binned spectra. The  $T_{\text{eff}}$  values for individual stars, divided as defined in §1 into metal-rich and metal-poor regimes at  $[\text{Fe}/\text{H}] = -1$ , populate two distinct regimes in correlations with phase, as shown in Figure 3. We have added curves to the figure to represent quadratic regression lines for the two metallicity groups. Model  $T_{\text{eff}}$ ’s of metal-rich stars are approximately 250 K hotter than those of metal-poor stars at all phases in the range  $0.2 < \phi < 0.6$ . Thus we confirm Skarka’s (2014) conclusion that metal-rich RRab stars are hotter than metal-poor RRab stars at a given  $B - V$  color.<sup>6</sup>

The temperatures and gravities are correlated with metallicities, as illustrated in Figure 4. Solid black lines denote linear regressions of the quantities using the entire metallicity range. The horizontal dashed lines denote mean values of the metal-poor and metal-rich stars. Standard deviations of these regressions for  $T_{\text{eff}}$  and for  $\log g$ , listed in Table 2 are indistinguishable, i.e., simple statistical analysis offers no guidance about choice of regressions. The physical bases for the natures of the correlations are uncertain. We defer further discussion of these two different statistical representations to §5.

The most metal poor star in our sample, X Ari ( $[\text{Fe}/\text{H}] = -2.6$ ), lies closer to the horizontal regressions for  $T_{\text{eff}}$  and  $\log g$ . Data for additional very metal-poor stars collected and analyzed in a uniform way may help to resolve this uncertainty in choice of regressions. We are aware of three such stars: NR Lyr,  $[\text{Fe}/\text{H}] = -2.54$  (Nemec et al. 2013); CS 22881-029,  $[\text{Fe}/\text{H}] = -2.75$ ; and CS 30317-056,  $[\text{Fe}/\text{H}] = -2.85$  (Hansen et al. 2011).

### 3.3. A Common Metallicity Scale for RRab Stars

Spectroscopic metallicities have been derived for RR Lyr stars beginning with the  $\Delta S$  parameter introduced by Preston (1959) to relate the strengths of the Ca II K line to the H I Balmer lines appearing on low-resolution spectra. Many observations and calibrations of  $\Delta S$  as a function of  $[\text{Fe}/\text{H}]$  have been published over the last several decades. The largest single source of K-line metallicities is the Lay94 the 302-star RRab survey. Previous RR Lyr large-sample high-resolution spectroscopic metallicity and abundance ratio surveys include: Clementini et al. (1995, 10 stars); Lambert et al. (1996, 18 stars); Fernley & Barnes (1996, 9 stars); For et al. (2011, 11 stars); Liu et al. (2013, 23 stars); Nemec et al. (2013, 41 stars); and Pancino et al. (2015, 18 stars). We relate the metallicities reported in those studies to the  $[\text{Fe}/\text{H}]$  values derived here, using Layden’s  $[\text{Fe}/\text{H}]$  values as the common baseline.

In Figure 5 we plot the differences between  $[\text{Fe}/\text{H}]$  values of various high-resolution studies (including our work) and those of Lay94 as a function of the  $[\text{Fe}/\text{H}]_{\text{Lay94}}$ . We have added simple linear regression lines to illustrate the mean trends, which have positive slopes in five of the seven cases. Inspection of this figure suggests that the most significant differences among most high-resolution studies are metallicity scale offsets.

To attempt to merge together all of the high-resolution studies, we first repeated the analyses of Clementini et al. (1995) and Pancino et al. (2015), using only lines in common with our work. We adopted their published  $EW$ s and our transition probabilities, and derived model parameters in the manner described in §3.1. In general our results were not significantly different than theirs.

<sup>6</sup> Skarka’s (2014) mean  $(B - V)_0$  colors are strongly correlated with those of Blanco (1992). The latter were calculated for the phase interval  $0.58 < \phi < 0.80$ . More recent studies, e.g., Jurcsik (1998), use mean color definitions derived from all parts of RR Lyr pulsational cycles including the hotter phases near  $\phi = 0$ . These mean colors are, therefore, bluer than the intrinsic colors used by Blanco to estimate interstellar reddening.

Then we shifted the  $[\text{Fe}/\text{H}]$  values of other studies onto our scale by using the regression lines shown in Figure 5, and updated regression fits to reflect our new analyses of Clementini et al. (1995) and Pancino et al. (2015) metallicities to calculate the offset between the other studies and ours at a metallicity  $[\text{Fe}/\text{H}]_{\text{Lay94}} = -1.25$ . This metallicity point is of course arbitrary but is approximately in the middle of the observed RR Lyr metallicity distribution. In Figure 6 we redraw Figure 5 with the re-analyses and applied  $[\text{Fe}/\text{H}]$  offsets. Then all high-resolution analyses are merged in Figure 7, and we add an additional point to include the  $[\text{Fe}/\text{H}]$  value for the eponymous star RR Lyr from the analysis by Kolenberg et al. (2010). There is general agreement on the relationship between high-resolution spectroscopic metallicities and the Lay94 values, and reasonably small scatter in this relationship. We stress that this exercise is not intended to be advocacy for our own RR Lyr metallicity scale. It simply suggests that with small scale shifts the  $[\text{Fe}/\text{H}]$  values of major RR Lyr high-resolution studies can be brought into good agreement.

Two stars deserve special comment because they help anchor the high and low ends of the RR Lyr metallicity scale. As such they have been well represented in past and present analyses. At the very metal-poor limit there is X Ari, with  $[\text{Fe}/\text{H}]_{\text{Lay94}} = -2.40$ . There is some discord among the high-resolution results:  $[\text{Fe}/\text{H}] = -2.50$  (Clementini et al. 1995, or  $-2.51$  in our reanalysis);  $-2.47$  (Lambert et al. 1996);  $-2.74$  (Nemec et al. 2013);  $-2.14$  (Pancino et al. 2015, or  $-2.20$  in our reanalysis); and  $-2.60$ , this study. From all five studies,  $\langle[\text{Fe}/\text{H}]\rangle = -2.49$  with  $\sigma = 0.22$ . Application of the scale offsets described above does not significantly shrink the total envelope of values, as can be seen in the lower panel of Figure 7. The revised high-resolution mean value is  $\langle[\text{Fe}/\text{H}]\rangle = -2.61$  with  $\sigma = 0.25$ . The shift from  $[\text{Fe}/\text{H}]_{\text{Lay94}}$  for X Ari is in agreement with the general trend line of our analysis, but renewed attention to this star would be welcome.

SW And is one of the most metal-rich RR Lyr stars with  $[\text{Fe}/\text{H}]_{\text{Lay94}} = -0.38$ . Most high-resolution studies report higher metallicities for this star, but with scatter:  $[\text{Fe}/\text{H}] = -0.06$  (Clementini et al. 1995, or  $-0.24$  in our reanalysis);  $-0.26$  (Fernley & Barnes 1996);  $-0.32$  (Lambert et al. 1996);  $-0.07$  (Liu et al. 2013); and  $+0.20$  (Nemec et al. 2013). The means before and after re-analyses and offsets are  $\langle[\text{Fe}/\text{H}]\rangle = -0.10$ ,  $\sigma = 0.20$ , and  $\langle[\text{Fe}/\text{H}]\rangle = -0.27$ ,  $\sigma = 0.14$ ; for this star the high-resolution analyses come into better accord with one another.

With the scale shifts described above, a common relationship emerges between the high-resolution multi-star metallicity surveys considered here and the Lay94 K-line metallicities. Our own data indicate that  $[\text{Fe}/\text{H}]_{\text{highres}} = 1.100 \times [\text{Fe}/\text{H}]_{\text{Lay94}} + 0.055$ . Future high-resolution studies can and should revisit this relationship, which provides an important calibration for K-line surveys that now can be efficiently conducted for large samples of Galactic and extragalactic stellar systems.

### 3.4. Relative Abundances of Other Elements

In §3.1 we described the derivation of relative abundances of several elements that can be studied even with moderate  $S/N$  spectra of metal-poor RR Lyr stars; see Table 4. Here we compare our  $[\text{X}/\text{Fe}]$  values to those reported by other abundance studies of RR Lyr stars and by several surveys of non-variables over a wide metallicity range. In Figure 8 we plot  $[\text{X}/\text{Fe}]$  ratios as a function of metallicity from: (b) this study (black dots); from other RR Lyr abundance studies (Clementini et al. 1995, Fernley & Barnes 1996, Lambert et al. 1996, Liu et al. 2013, and Pancino et al. 2015; red dots); and (c) several large-sample studies of Galactic thin and thick disk main sequence and subgiant stars (Reddy et al. 2003, Reddy et al. 2006, Bensby et al. 2014 green dots), and of Galactic halo low metallicity stars of various evolutionary states (Roederer et al. 2014; also green dots). Relative abundance ratios are to first order insensitive to absolute metallicity scale, so we go through the data in Figure 8, species by species.

In considering the data of Figure 8, note first that abundance ratios determined in our work are consistent with those reported in other RR Lyr studies. Second, for most elements this agreement extends also to comparisons between the RR Lyr and non-variable stars. Third, the RR Lyr metal-poor abundance ratios are always in accord with those of non-variable stars. However, there are a couple of discordant cases to be noted among the abundances of metal-rich stars, and so here we will go through the figure on species-by-species basis.

- *Ca*, Figure 8 panel (a): All reported abundances are based on Ca I lines, which are plentiful (our values come from eight lines on average; Table 4). The  $[\text{Ca}/\text{Fe}]$  ratios of RR Lyr stars agree very well with those from other stellar sample over the entire metallicity range.
- *Sc*, Figure 8 panel (b): All reported abundances are based on a handful of Sc II lines. For halo stars the Sc abundances of RR Lyr stars agree well with their non-variable counterparts, but for disk stars the  $[\text{Sc}/\text{Fe}]$  values for RR Lyr stars are 0.3–0.4 dex smaller than those of disk main sequence and subgiant stars. One expects  $[\text{Sc}/\text{Fe}] \simeq 0$  at  $[\text{Fe}/\text{H}] \simeq 0$ , so the RR Lyr abundances surely are wrong here. Resolution of this problem, shared much more mildly by Ti II and Ba II (see below), is beyond the scope of this paper. Note that the

first ionization potential of Sc is low ( $IP = 6.56$  eV), ensuring that  $N_{ScII} \gg N_{ScI}$ , as is the second ionization potential (12.80 eV, lower than even that of hydrogen, 13.60 eV). It is entirely possible that limitations of standard abundance analyses applied to the variable RR Lyr stars are appearing in the LTE calculations of Sc ionization.

- *Ti*, *Figure 8 panel (c)*: We have chosen to plot only abundances from Ti II here, since in general this species has stronger transitions than does Ti I. There is a small Ti abundance offset,  $\simeq 0.2$  dex, between RR Lyr and non-variable disk stars.
- *Cr*, *Figure 8 panel (d)*: We were only able to measure a few lines of each Cr species, and so we chose to average their abundance ratios for this figure. Within the uncertainties of RR Lyr analyses, there is agreement with the non-variables at all metallicities.
- *Mn*, *Figure 8 panel (e)*: The well-known sharply declining  $[Mn/Fe]$  values with decreasing metallicity are reproduced well in RR Lyr abundance surveys. There are too-few points for stars with  $[Fe/H] < -2$  to draw firm conclusions on a possible negative offset relative to non-variable stars in this metallicity regime.
- *Ba*, *Figure 8 panel (f)*: The agreement between RR Lyr abundance ratios and those of non-variables is satisfactory, given the large star-to-star scatter among all samples.

In summary, the abundance ratios derived for our RR Lyr sample are mostly consistent with those seen in other stellar populations; further investigation of Sc and Ba would be welcome.

#### 4. RADIAL VELOCITY AND $H\alpha$ FLUX MEASUREMENTS

We accumulated 50-200 spectra for each program star. These allow us to examine radial velocity variations of the metallic lines and the  $H\alpha$  line with pulsational phases, and to quantify the strengths of the emission component of the  $H\alpha$  lines that occurs near phase  $\phi \simeq 0.9$ . We did not consider the Blazhko stars BS aps, UV Oct, V1645 Sgr, and AS Vir here, leaving 24 stars for these analyses. CD Vel has been identified as a Blazhko variable (Szczygiel & Fabrycky 2007) with  $P_{Bl} = 66.25$  d. We included it in our analysis of stable RRab stars because its radial velocity behavior appeared to be stable during the entire time interval of our observations ( $\Delta HJD = 1070$  d); see Figure 9.

Below we describe the derivation of velocities and emission measures. For each star we show the results via three plots as a function of pulsation phase, as displayed in Figure 9. The left panel contains the radial velocities of the metallic lines and  $H\alpha$ . The velocity range shown is always  $160 \text{ km s}^{-1}$  with the boundaries shifted appropriately for each star. The middle panel has our  $H\alpha$  emission measures, with the vertical ranges chosen to clearly show emission for each star. The right panel shows the ASAS V-band photometry, phased with the period written in the panel legend. The range in  $V$  is always 1.6 magnitudes, shifted for display purposes. Also in the legend is the stellar metallicity, computed as the mean of  $[Fe/H]$  values derived from Fe I and Fe II lines (Table 4). We show in the manuscript only the data for X Ari, and plots for the other stars can be accessed in on-line files.

##### 4.1. Radial Velocities

Thirteen orders of each RR Lyrae spectrum spanning the wavelength interval  $\lambda\lambda 4000\text{--}4600 \text{ \AA}$  were flattened and stitched together by use of an IRAF script prepared by Ian Thompson (private communication). This is the same spectral interval used in the radial velocity investigations of Preston & Sneden (2000); Chadid & Preston (2013). Radial velocities of metal lines in these spectra were obtained by use of the IRAF/fixcor package. Masks centered on  $H\delta$  and  $H\gamma$  were employed to avoid deleterious broadening of the cross-correlation function by these wide, strong lines. The reference spectrum for metal-lines is that of CS 22874-009 for which we adopted  $RV = -36.6 \text{ km s}^{-1}$ , the value used by Preston & Sneden (2000). The reference spectrum for  $H\alpha$  is that of the metal-poor giant CS 22892-052 for which we adopted  $RV = +14.2 \text{ km s}^{-1}$ . This particular value contributed to an appreciable systematic correction noted in the following paragraph.<sup>7</sup> Outputs of the fixcor package include VHELIO, the radial velocity corrected for the earth's orbital and diurnal motions, and HJD, the Heliocentric Julian Date needed to calculate pulsation phases.

Numerous observations of HD140283, our primary radial velocity standard, for which  $RV = -170.9 \text{ km s}^{-1}$  (Kollmeier et al. 2013) were used to apply a systematic correction of  $-2.9 \text{ km/s}$  to measured  $H\alpha$  radial velocities. Spectra of du Pont echelle order 53, which contains  $H\alpha$  near its center, were prepared for measurement as follows. For each stellar

<sup>7</sup> The tentative low-amplitude velocity variation of CS 22892-052 suggested by Preston & Sneden (2001) has not been confirmed by additional observations and analyses.

spectrum we made an average spectrum of adjacent orders 52 and 54. We divided order 53 by a spline fit to the continuum of this average spectrum, thus obtaining a flattened normalized spectrum of order 53 in which fluxes at  $H\alpha$  can be measured in units of the continuum flux at  $6560 \text{ \AA}$ . These spectra were also used to measure the radial velocity of  $H\alpha$ .

We used the Gaussian fitting function of IRAF/fxcor package to locate the centers of  $H\alpha$  absorption features. In the course of our measurements we discovered that the ‘‘Doppler’’ core of the  $H\alpha$  line is noticeably asymmetric during substantial fractions of pulsation cycles, the slope of one wing (sometimes red, sometimes violet) being greater than the other. In all such cases we fit a Gaussian to the flux minimum and the *steepest* wing of the profile, arbitrarily attributing the other broader wing to unspecified asymmetry in line-of-sight gas motion, perhaps due to weak shocks at some pulsation phases. We don’t *know* why the profiles are asymmetric, but we needed a rule in order to measure them in a consistent manner. For a description of the shock complexity that accompanies RR Lyrae pulsation see the observational evidence presented by Chadid & Preston (2013). The magnitude of effects resulting from use/non-use of our measurement procedure is almost always less than  $2 \text{ km s}^{-1}$ , and usually less than  $1 \text{ km s}^{-1}$ , metrics that characterizes the inherent uncertainty of  $H\alpha$  radial velocity estimates made with the du Pont echelle spectrograph.

#### 4.2. $H\alpha$ Emission Flux Measurements

Emission flux measurements were made with the IRAF/plot package as sums of pixel counts in the  $H\alpha$  profile above a reference continuum. When the emission profile lies entirely above the continuum, the measurement is unambiguous. However, when the emission is flanked by violet and red absorption components, an inescapable ambiguity arises about the portions of the flux between the absorption components that are due to overlapping absorption wings and those due to bona fide line emission. In instances when the flux maximum between absorption components lies below the continuum level, skeptics may deny the existence of *any* emission. Justification for emission measurements in such cases rests on an appeal to phase continuity; namely, it would be unreasonable to suppose that emission ceased exactly at the moment when the apparent emission peak fell below continuum level. On the other hand, deciding exactly when to discontinue emission measurements and to begin measurement of violet-shifted absorption velocities requires a subjective judgment that we base on apparent radial velocity. When a violet absorption minimum first appears, its apparent velocity is strongly negative relative to the velocity measured minutes later when the violet and red minima have equal depths. Examples of rapidly increasing sequences of such ‘‘apparent velocities’’ near phase 0.9 can be seen in left panels of a number of stars in Figure 9. We deliberately included such (spurious) measures in the RV plots to illustrate how we decided when to treat the apparent violet minima as valid indicators of mass motion in the atmosphere. In our view the proper moment occurs when a cusp in the expanding velocities occurs near mid-rising light. Prior to that moment we regard the violet-displaced flux minimum in the profile merely as an *apparent* absorption minimum located between the violet Stark absorption wing and the violet wing of approximately undisplaced central emission.

During primary light rise Balmer line emission (different in each star and overlain by red-displaced absorption) appears briefly in many RRab spectra, as illustrated in Figure 6 of Preston & Paczynski (1964). We use the emission flux in the violet wing of the  $H\alpha$  profile as an admittedly imperfect proxy for the total (un-measurable) flux. Measurements of this  $H\alpha$  flux were made as follows. A reference continuum was chosen at the violet-displaced flux minimum in the  $H\alpha$  profile, as illustrated by the horizontal red line in Figure 10. Uncertainties of unknown magnitude associated with this choice of reference level undoubtedly occur from exposure to exposure during primary light rise because of rapidly changing contributions from two absorption profiles to the total flux. Flux counts in the emission profile above the reference level (the red horizontal line in Figure 10), are expressed in units of the local continuum fluxes at the phases of observation. To obtain true relative fluxes it would be necessary to multiply the plotted fluxes by the phase-dependent continuum fluxes at  $6560 \text{ \AA}$ , which increase rapidly during the  $H\alpha$  emission phase sequences.

Table 5 contains a summary of quantities derived from the radial velocity and flux measurements. For five stars we list two metal velocity amplitudes that differ by as much as  $4 \text{ km s}^{-1}$  in different cycles. Our survey data do not provide enough information to determine whether these velocity differences are due to low-amplitude Blazhko modulation or to ‘‘irregularity’’ of the sort reported by Chadid (2000). For consistency we use the largest of these values in all graphical displays that follow.

#### 4.3. Photospheric motion parameters

From a du Pont echelle heliocentric radial velocity  $V_r(t)$ , we derive a pulsational velocity  $\dot{R}(t)$  in the stellar rest frame using:

$$\dot{R}(t) = -p(V_r(t) - V_*) \quad (1)$$

where  $p$  is the value of the correction factor for geometrical projection and limb darkening and  $V_*$  the center-of-mass velocity. Because we derive radial velocities from metallic lines formed near the photosphere, the pulsational velocity  $\dot{R}(t)$  is approximately that of the photosphere. We adopt in this study the projection factor  $p = 1.36$ . Use of this approximation is discussed by Chadid & Preston (2013). Using polynomial fitting, we calculate the  $\gamma$ -velocity as the average value of the heliocentric radial velocity curve over one pulsation period. The derivative of  $\dot{R}(t)$  gives the dynamical acceleration  $\ddot{R}(t)$  of the stellar surface layer in which metallic absorption lines are formed:

$$\ddot{R}(t) = d\dot{R}(t)/dt \quad (2)$$

Performing the integration of  $\dot{R}(t)$ , we derive the photospheric radius variation  $\Delta R(t)$ :

$$\Delta R(t) = R(t) - R_{ph} = \int_0^t \dot{R}(t) dt \quad (3)$$

where  $R_{ph}$  is the mean photospheric radius of the star.

Radius and acceleration curves are respectively computed from integration and derivative of radial velocity curve. During the pulsation period ( $0 < \phi < 1$ ) the gaps in the measurement data have been interpolated linearly, and, in order to minimize the noise, the raw radial velocity curves have been convoluted by a sliding window of  $\Delta\phi = 0.1$  width.

Table 6 contains a summary of photospheric motion parameters derived from the photospheric heliocentric radial velocity of the metal-poor and metal-rich RRab stars. The acceleration and the radius variation curves for individual metal-poor and metal-rich RRab stars, as well as the means for the two groups, are shown in Figure 11. The acceleration curves exhibit two significant peaks. An acceleration peak (hereafter primary acceleration) occurs near phase  $\phi = 0.90 \pm 0.02$ ; it corresponds to the phase of minimum radius. A *much* smaller secondary acceleration peak occurs near phase  $\phi = 0.72 \pm 0.02$ . These secondary accelerations are clearly visible for several of the stable RRab stars in Figure 5 of Chadid & Preston (2013). Any acceleration associated with the *lump*<sup>8</sup>, *rump*, and *jump* in the RV curve (Chadid et al. 2014) that may be present around  $\phi = 0.30$ ,  $\phi = 0.10$  and  $\phi = 0.70$  respectively are at or below the level of detection.

Chadid & Preston (2013) call primary acceleration the dynamical gravity of the star. We derive the average of the gravitational acceleration,

$$g = G \frac{M}{R^2} \quad (4)$$

where  $G$  is the gravitational constant ( $G = 6.67 \times 10^{-11}$ ), and  $M$  and  $R$  are respectively the mass and radius of the star.

Figure 11 shows that almost all metal-poor RRab stars have radius variations larger and primary accelerations smaller than those of metal-rich RRab stars. Mean radii of metal-poor and metal-rich RRab stars occur at very nearly the same phases,  $\phi = 0.65 \pm 0.02$  during infall and  $\phi = 0.12 \pm 0.02$  during outflow. The amplitude of radius variation is larger by 50% in the metal-poor as it is in the metal-rich RRab stars. The radius variations indicate that RRab stars are relatively extended stars for about half of their pulsation cycles; the minimum radius occurs near  $\phi = 0.92 \pm 0.02$  and the maximum value at  $\phi = 0.38 \pm 0.02$ .

de Boer & Maintz (2010) claim to have detected a rapid collapse phenomenon in the atmosphere of RRab stars by the use of multichannel Strömgren photometry. They suggest that at phase  $\phi = 0.90$  the atmosphere begins to collapse, quickly reaching a high gas density; then within a small phase interval  $\Delta\phi = 0.10$ , the atmosphere expands again. No rapid collapse phenomena associated with the radius variation as suggested by de Boer & Maintz (2010) are detected in our spectroscopic data.

The physical origin of the primary acceleration, the dynamical gravity of the star, is due to the  $Sh_{H+He}$ , the main shock produced by the  $\kappa$  and  $\gamma$  mechanisms, processes based on the effects of radiative opacity in  $He^+$  and  $He^{++}$  ionization zones that drive the pulsational instability in RRab stars (Cox 1980). The secondary acceleration is caused by the shock  $Sh_{PM3}$ , described in Chadid et al. (2014), that produces compression heating. We suggest that primary acceleration is a better proxy for the intensity of the  $Sh_{H+He}$  main shock. Accordingly, we use rise time, the very short time interval of the descending branch of the radial velocity curve to characterize the shock intensity.

Nearly all RRab stars of this study possess more or less prominent secondary radial velocity maxima, the elbow near phase  $\phi = 0.72 \pm 0.02$ . The phase and visibility of this maximum vary from star to star. It occurs late for WY Ant,

<sup>8</sup> The terms *hump*, *lump*, *rump*, and *jump* follow the nomenclature of Chadid et al. (2014)

and is indistinct for DT Hya and Z Mic. The secondary acceleration is largest for the metal-rich star HH Pup, which also exhibits the largest dynamical gravity. Metal-poor star VY Ser has the lowest dynamical gravity in our sample.

We collect all of the derived motion parameters in Figure 12, using the primary acceleration (dynamical gravity) as the common variable on the figure’s horizontal axis. The various correlations seen in Figure 12 will be discussed in subsequent sections. Inspection of this figure show that several motion parameters have fundamentally different relationships with primary acceleration, such as radius variation (panel b), duration of H $\alpha$  doubling  $\Delta t$  (panel d, discussed in §7.1), and H $\alpha$  velocity amplitude  $\Delta RV_{H\alpha}$  (panel e). In contrast, the other motion parameters show a single trend but different (albeit overlapping) regions occupied by the metal-poor and metal-rich RR Lyr stars.

## 5. EMISSION LINES AND SHOCK WAVES

Shock pulsation models (Zeldovich & Raizer 1966) suggest that the shock structure can be subdivided into five principal zones with different physical characteristics: the precursor zone, the shock front, the thermalization zone, the ionization zone, and the zone of the cooling wake which is partially transparent in the Balmer and weak spectral lines. The wake zone, just behind the shock front, is a relatively narrow region in comparison with the photospheric radius (Chadid 2011). The evolution of RR Lyrae H $\alpha$  line profiles gives crucial information about nonlinear dynamics in the extended atmosphere above the wake zone. The wings of H $\alpha$  lines are formed deep in the atmosphere while the line cores are formed higher. We study the Doppler effect in these cores.

Chadid et al. (2014) report photometric evidence for multiple shock waves crossing the envelope of the RR ab Blazhko star S Arae. These shocks,  $Sh_{PM1}$ ,  $Sh_{PM}$ ,  $Sh_{PM2}$ ,  $Sh_{PM3}$ , and  $Sh_{H+He}$  appear respectively during the *jump*, *lump*, *rump*, *bump* (secondary acceleration) and *hump* (primary acceleration) in the light curve, with different amplitude and physical origin. When shocks traverse the envelope, they heat the sub-photospheric gas that caused a local decrease of the opacity and consequently they induce a luminosity increase in the light curve. Chadid et al. (2014) proposed a new shock propagation scenario and showed that during the time interval of the ascending branch of the radial velocity curve all shocks are receding in Eulerian coordinates system while they are advancing shocks in the Lagrangian coordinates system. The brightest H $\alpha$  emissions observed during the *hump* and *bump* are directly produced in the radiative wake of respectively the  $Sh_{H+He}$  main shock caused by the  $\kappa$  and  $\gamma$  mechanisms, while the  $Sh_{PM3}$  is caused mainly by collisions and compression waves. The H $\alpha$  absorption lines show doubling of their cores during the *hump* (primary acceleration). According to the classical Schwarzschild doubling effect (Schwarzschild 1952), the phenomenon can be explained by the propagation of the main shock,  $Sh_{H+He}$ . No doubling of the H $\alpha$  absorption lines has been detected during the *bump* in the light curve heretofore.

## 6. FIRST DETECTION OF H $\alpha$ LINE-DOUBLING DURING THE BUMP

We have obtained clear evidence of H $\alpha$  line-doubling during the photometric *bump* associated with the secondary acceleration in two of the brightest RRab stars in our sample, WY Ant and RV Oct. It begins near the phase of violet-displaced H $\alpha$  emission reported by Gillet & Crowe (1988). We use the spectra of RV Oct here for illustrative purposes. Marginally resolved H $\alpha$  line-doubling during the phase interval 0.63–0.85 is common, if not ubiquitous, among the the metal-poor RRab stars of our sample. It occurs during the inward motion of a shock in the Eulerian coordinates system.

### 6.1. Apparent ballistic acceleration and deceleration

We suspect that the violet emission edge of the H $\alpha$  that first appears near phase  $\phi = 0.62 \pm 0.02$  in the top panel of Figure 13 is responsible for the small, apparent increase in radial velocity seen in the bottom panel of Figure 13 at this phase. This emission pushes measured radial velocities to spuriously large values, enhancing the brief secondary velocity maximum. The apparent deceleration, the *elbow*<sup>9</sup>, that follows is due to heretofore unresolved line-doubling during the  $Sh_{PM3}$  shock. A line component of longer wavelength produced by ballistic infalling gas also appears suddenly at phase 0.63 and strengthens as the original line weakens and gradually disappears. Because IRAF/xcor does not clearly resolve this line-doubling in most of our spectra, we usually do not detect the velocity discontinuity depicted schematically by the blue lines in the bottom panel of Figure 13. Note that both line components are formed by infalling gas at the interface of the  $Sh_{PM3}$  ballistic shock. Such doubled profiles are not present in any of our spectra of metal-rich RRab stars.

### 6.2. Bump line-doubling mechanism

<sup>9</sup> The term elbow follows the nomenclature of Chadid & Preston (2013)

The  $Sh_{PM3}$  ballistic shock (Chadid et al. 2014) crosses the inward moving atmosphere during the phase interval  $\Delta\phi$  [0.63,0.85].  $H\alpha$  line emission is produced in the radiative wake of the ballistic shock. Figure 14 illustrates schematically the sequence of  $H\alpha$  profiles during the phase interval 0.62–0.76. The  $H\alpha$  profile shows first a redshifted absorption line (hereafter original line). At phase  $\phi = 0.62$  a blueshifted emission appears while the velocity of the original line increases and its residual intensity decreases. A new second redshifted absorption line appears at phase  $\phi = 0.63$  with a velocity greater and a residual intensity smaller than the original line. At phase  $\phi = 0.66$ , the residual intensity of the second redshifted line increases to be equal to that of the original line. At phase  $\phi = 0.73$ , the second redshifted line strengthens as the original line weakens and gradually disappears.

We interpret these variations in the  $H\alpha$  profile during the bump in the light curve as follows. We assume that the  $Sh_{PM3}$  ballistic shock crossing the infalling  $H\alpha$  line forming zone has an inward motion in the Eulerian rest frame although is moving outward in the mass Lagrangian coordinates system, and that its existence is strongly dependent on the amplitude of the ballistic motion. Initially the velocity of  $Sh_{PM3}$  is not large enough to produce resolved doubling. The shock, moving outward through mass shells, is accelerated during its propagation; consequently a second redshifted absorption component is observed with a higher velocity than the original line. Its residual intensity increases as the original line weakens at phase  $\phi = 0.66$ . At this time the  $H\alpha$  doubling is clearly visible and the shock amplitude is near  $50 \text{ km s}^{-1}$ . The speed of sound is almost entirely dependent on its temperature, being roughly equal to  $0.11 \times \sqrt{T_{eff}}$  in  $\text{km s}^{-1}$  units. Adopting  $T \sim T_{eff} = 6050 \text{ K}$  for RV Oct (Table 3), the Mach number of the the shock  $Sh_{PM3}$  is approximately 8.

Thus a shock Mach number around 8 is necessary to produce the  $H\alpha$  line-doubling phenomenon. Later at phases 0.76–0.85, the original line gradually disappears. At phase  $\phi = 0.85$ , the shock leaves the  $H\alpha$  forming zone as the star approaches the phase of the minimum radius. Soon thereafter, the shock  $Sh_{H+He}$ , associated to the primary acceleration, emerges from the photosphere and reverses the motion of infalling atmospheric layers.

The weak  $H\alpha$  emission, associated with the inward shock  $Sh_{PM3}$ , appears blue-shifted, which is inconsistent with what we expect to see, namely red-shifted emission. This is puzzling. We conclude that more than one mechanism must be at work to produce the observed profile. We suggest that an atomic mechanism, some combination of Stark and Doppler broadening, and a geometric mechanism – some unanticipated motions of gas layers – may be responsible. We simply do not know how these mechanisms combine to produce what is observed.

In closing this section we call attention to the visibility of the elbow in the metal-RV curves of Figure 9. The elbow is well-marked, or at least identifiable in most metal-poor RRab stars. However, it is not present in metal-rich ST Vir, DX Del, V445 Oph, AV Peg, and AN Ser, and it is only marginally visible in large-amplitude HH Pup and W Crt. We shall see in §7 that this distinction is related to the different atmospheric extents of metal-poor and metal-rich atmospheres.

## 7. COMPARISON OF DYNAMICS IN METAL-RICH AND METAL-POOR RRAB ENVELOPES

### 7.1. Difference in upper-atmosphere structure

The strong albeit imperfect correlation of V-light amplitude with metallic line RV amplitude in Figure 15 shows, first of all, that these two amplitudes are equally acceptable indicators of RRab pulsation amplitude. Residuals of individual stars in these regressions can be understood as a combination of errors in the amplitude estimates and small (non-Blazhko) irregularities in pulsation amplitudes in some stars (Chadid 2000). In particular, the rms scatters of ASAS  $V$  magnitudes that produce the  $V$  light amplitudes in Table 5 are strongly correlated with apparent magnitude because signal-to-noise decreases with decreasing luminosity in the ASAS program. The well-known period *versus* light amplitude relations among RRab stars (Clement & Shelton 1999) and their associated period *versus* velocity amplitude relations undoubtedly contribute to the scatter as well. Investigations of the latter are beyond the scope of this paper. Slopes of the regressions calculated separately for metal-rich (red) and metal-poor (blue) in this diagram differ by less than the sum of their standard errors, regardless of the choice of independent variable in the least squares solutions. Thus metal-poor and metal-rich RRab stars share a common relation between luminosity amplitude and photospheric velocity amplitude.

However, the  $H\alpha$  lines of metal-poor and metal-rich stars which are formed at very low optical depths (§5) behave very differently in metal-poor and metal-rich stars, as illustrated in Figure 16. The  $H\alpha$  velocity amplitudes of the metal-rich stars are systematically smaller by  $\sim 20 \text{ km s}^{-1}$  than those of metal-poor stars at a given metal velocity amplitude. The velocity structures and geometrical extents of the outer atmospheres of the two groups must be very different.

The durations of double  $H\alpha$  lines in the two abundance groups shown in Figure 17 provide an additional indication

of different atmospheric structures. We define duration as the time interval  $\Delta t$  during which IRAF/splot can identify two absorption minima in the  $H\alpha$  profile. The durations are markedly longer in stars with large  $H\alpha$  emission fluxes. We note that three of the four stars with *no* observed  $H\alpha$  emission flux (AV Peg, V445 Oph, and W Crt) have the very short periods that attracted Kukarkin's (1949) attention long ago. The fourth, DX Del ( $P = 0.473\text{d}$ ), has the lowest light and RV amplitudes in our metal-rich sample.

The ranges in appearance and duration of line-doubling is illustrated in the montages of  $H\alpha$  profiles for metal-rich AV Peg and metal-poor RV Oct in Figure 18. The profiles of AV Peg are typical of the four stars mentioned above, i.e. they are devoid of  $H\alpha$  emission in our du Pont echelle spectra. A violet absorption wing turns into a resolved absorption feature that replaces the red component on the short time scales plotted in Figure 17. In AV Peg line doubling can be seen only in the brief interval from  $\phi = 0.93$  to  $\phi = 0.96$ ,  $\Delta t = 0.03 P = 1000\text{s}$ , corresponding to 3% of pulsation period. The same datum for RV Oct is  $\Delta t = 0.17 P = 8400\text{s}$ , corresponding to 17% of pulsation period; the durations differ by a factor  $\sim 8$ . These durations are measures of the times that out-flowing gas sweeps up and reverses the flow of in-falling gas. They define the lifetime of the  $Sh_{H+He}$  main shock in the upper atmosphere. The lifetimes of the main shocks in metal-poor and metal-rich stars differ by a factor  $\sim 8$ . For fluxes less than 1 continuum unit, the metal-poor durations exceed metal-rich durations by a factor of two or less. Note, however, that durations as large as  $0.12\text{d} \sim 10000\text{s}$  occur among the metal-poor stars plotted in Figure 17.

### 7.2. Difference in photospheric structure

The panel (d) of Figure 12 tells us that large photospheric dynamical gravities (i.e., strong shocks) in the photospheres of metal-rich stars are of short duration, while weaker shocks in metal-poor stars are of longer duration. We make a dynamical gravity division between the metal-poor and metal-rich families near to  $\ddot{R}=30\text{ km s}^{-2}$ . To this, we add the well-marked correlation between  $H\alpha$  flux and duration of the weaker shocks of metal-poor stars shown in Figure 17. Finally, recall that the photospheric radius variation is larger for the metal-poor RRab stars than for the metal-rich stars (bottom panel of Figure 11); the average difference in the panel (b) of Figure 12 is approximately  $\Delta R = 0.17 R_{\odot}$ .

All the regressions in Figure 12 indicate that dynamical gravity, the primary acceleration, is the empirical, unifying, causal parameter of the various observed envelope phenomena. Used as independent variable it produces simple linear regressions for secondary acceleration, radius variation, rise-time, duration of  $H\alpha$  doubling, and hydrogen and metallic radial velocity amplitudes. The slopes and intercepts of the metal-rich regressions (red-straight lines) are different from those of their metal-poor counterparts (blue-straight lines). The differences between the metal-rich linear regressions and those of their metal-poor counterparts are more pronounced in the upper-atmospheric parameters (duration of  $H\alpha$  doubling,  $H\alpha$  radial velocity amplitude and  $H\alpha$  emission) than those of the photosphere (secondary acceleration, metal radial velocity amplitude and rise-time). Finally, the radius variation is larger by a factor  $\sim 1.8$  for metal-poor stars than that of their metal-rich counterparts.

To conclude, the motions of the upper-atmospheric and near-photospheric regions exhibit very different behaviors, and these differences are more pronounced in metal-poor RRab stars than in their metal-rich counterparts.

### 7.3. Interpretation

Panel (a) of Figure 12 shows the regression between the secondary and primary accelerations for metal-poor and metal-rich RRab: the stronger the dynamical gravity the more important is the secondary acceleration. Both groups share a similar physical process of the amplification of the secondary acceleration with the primary acceleration which indicates dynamical coupling interplay between the  $Sh_{H+He}$  main shock and the  $Sh_{PM3}$  ballistic shock. The greater the dynamical gravity, the larger is *Mach* number  $Sh_{H+He}$  that causes higher level of dynamical imbalance, i.e., the non-synchronization of motions in the upper and lower photospheric layers. Stronger collision induce higher supersonic motion,  $Sh_{PM3}$ . Thus secondary acceleration becomes more important. Two distinct correlations between metal-line (near-photospheric) radial velocity amplitude and primary acceleration exist for both metal-poor and metal-rich RRab stars (panel (f) of Figure 12). The amplitude of the photospheric ballistic motion is larger when the photosphere is crossed by a stronger shock, i.e., the more important primary acceleration, the larger is the metal radial velocity amplitude. The comparison of primary accelerations in the top panel of Figure 11 demonstrates that the intensity of the  $Sh_{H+He}$  main shock is more important in the photospheres of metal-rich stars than those of metal-poor stars.

The most striking characteristic of the ballistic photospheric motion is its greater magnitude in metal-poor relative to metal-rich RRab stars (Figure 12). Longer period implies longer ballistic motion. The greater extensions of the metal-poor envelopes complicates their atmospheric motions; the non-synchronization effect greatly changes atmospheric motion structure and creates chaotic behavior, mainly in the upper atmospheres. Moreover, the region of formation of spectral lines is greatly enlarged with concomitant effects on line profiles. This enlarged region of line formation

in metal-poor stars is the origin of the greater duration of  $H\alpha$  doubling (Figure 12, panel (d) ),  $H\alpha$  radial velocity amplitude (panel (e) of Figure 12) and the peak  $H\alpha$  emission flux.

$H\alpha$  emission is generally weaker in metal-rich RRab stars (Figure 19). No emission could be detected in four of the eight metal-rich RRab stars in our sample (AV Peg, V445 Oph, ST Vir and DX Del), and the strongest emission in the remaining four occurred in the lowest metallicity star of the metal-rich group (UU Vir,  $[\text{Fe}/\text{H}] = -0.93$ ). We attribute this metallicity effect to the fact that the metal-poor RRab atmospheres are more extended, and the amplitudes of the ballistic motions of the metal-poor RRab atmospheres are greater than those of metal-rich RRab.

The bottom panel of Figure 19 shows that strongest  $H\alpha$  emission in RRab stars is restricted to those with the largest hydrogen radial velocity amplitudes. A threshold effect seems to be present: a steep gradient of  $H\alpha$  emission occurs near  $H\alpha$  radial velocity amplitude  $\sim 115 \text{ km s}^{-1}$ , when the duration of  $H\alpha$  line-doubling is  $\sim 10\%$  of the pulsation period. The emission flux increases abruptly when the dynamical gravity exceeds  $\ddot{R} \sim 20 \text{ km s}^{-2}$ , independent of the metallicity, pulsation period and radius variation. We call this phenomenon the hydrodynamic gradient. This mechanism applies to metal-poor and perhaps to metal-rich RRab stars as well. Only one metal-rich RRab star in our sample (UU Vir,  $[\text{Fe}/\text{H}] = -0.93$ ) shows this phenomenon, and it is the most metal-poor of the group. The hydrodynamic gradient mechanism is strongly dependent of the temperature and the gravitational acceleration of the star, and affects the stars with lower temperatures ( $< 6100 \text{ K}$ ) and slighter gravities ( $\log g < 1.9$ ) (Fig 4). Evidently the upper atmosphere reaches a high-hypersonic regime when the dynamical gravity exceeds  $\ddot{R} \sim 20 \text{ km s}^{-2}$ . Accordingly, we divide the metal-poor RRab stars into two types, type 1 and type 2, and we define four main shock regimes in the upper atmospheres of RR Lyrae stars:

1. Trans-sonic Regime: No hydrogen emission or line doubling is observed. This regime could characterize RRc and RRd.
2. Supersonic Regime: Hydrogen line doubling and only a very small or even no hydrogen emission is observed. This regime occurs mostly in the metal-rich RRab.
3. Hypersonic Regime: Additional He I emission line is observed. The temperature must be higher than  $10\,000 \text{ K}$ , with a threshold Mach number  $Mach_{\text{HeI}}$ . The hypersonic regime occurs in metal-poor RRab type 1 and a few metal-rich RRab with higher dynamical gravity.
4. High-hypersonic Regime: He II emission line is observed. The temperature and energy respectively higher than  $30\,000 \text{ K}$  and  $24.59 \text{ eV}$  are able to ionize a neutral helium atom with a threshold Mach number  $Mach_{\text{HeII}}$ . The atmosphere is very extended and a circumstellar envelope around the star may occur. This should characterize the metal-poor RRab type 2 that could be cooler and more convective. This regime has been already identified in two metal-poor RRab stars: AS Vir and V1645 Sgr (Preston 2011).

Finally, we consider briefly the  $H\alpha$  emission of RRab stars in the context of other post-main sequence pulsating stars. We note the absence of H emission in most classical Cepheids with periods less than 10 days, i.e., those Cepheids with lowest luminosity and least extended atmospheres. Among the remainder, the  $H\alpha$  emission of the metal-poor RRab stars is weaker than those seen in W Virginis, RV Tauri, and Mira stars. The latter families comprise a sequence of increasing luminosity and atmospheric extent. Wider atmospheric extension in these cooler pulsators is accompanied by larger Mach numbers of  $Sh_{\text{H+He}}$  and stronger shocks.

## 8. ARE METAL-RICH AND METAL-POOR RRAB TWO SEPARATE FAMILIES?

We suppose that metal-rich and metal-poor RRab stars belong to a single family of helium-core-burning horizontal branch stars. However, our study reveals strikingly different characteristics of these two subgroups. Their atmospheric dynamics and structure are different. This difference is typically more pronounced in the upper atmosphere. The differences in their atmospheres are induced by large differences in the mechanical energy of the ballistic motion and the strengths and locations of shock waves in the photosphere and upper atmospheric layers. Indeed, according to §5, the dynamical gravity and then the  $Sh_{\text{H+He}}$  main shock intensity are larger in the photospheres of metal-rich RRab than they are in those of metal-poor RRab. The  $Sh_{\text{H+He}}$  main shock always propagates outwards and its amplitude increases with height as the density of the gas decreases until dissipation mechanisms kill the shock. The  $Sh_{\text{H+He}}$  main shock strengthens as it propagates highly into regions of lower gas density and reaches high Mach numbers. The main shock intensity is larger in the upper atmospheres of metal-poor RRab than in those of metal-rich RRab.

Our spectroscopic results show that the gravitational acceleration and effective temperature are smaller in metal-poor RRab than in metal-rich. From these considerations we hypothesize that:

(1) unlike the metal-poor stars, the metal-rich stars lie close to the blue edge of the fundamental  $F$  mode instability region where the first overtone mode may disturb the fundamental mode by acting on the radiative loss of the  $Sh_{H+He}$  main shock. In fact, from our results, the effective temperature is smaller in metal-poor than metal-rich RR ab stars. Accordingly, we hypothesize that the metal-rich stars are close to the blue edge of the fundamental instability strip. On the other hand, we might hypothesize that metal-rich RR ab stars are affected by a disregarded first overtone mode. The small amplitude of this latter is unable to invoke the double mode behavior similar to Bailey's RRd and has no sign in the frequency spectra. This small first overtone excitation might generate a small perturbation that disturbs the  $\kappa$  and  $\gamma$  mechanisms process, and therefore might react on the radiative loss of the main shock. (2) The gravitational acceleration is smaller in metal-poor RR ab. Therefore the non-synchronization of their photospheric layers is less pronounced.

(3) The metal-poor stars lie closer to the cooler fundamental red edge, so their convective envelopes are deeper. The thicknesses of their compression zones are greater, which may explain why their photospheric radii and their radius variations are larger. The  $Sh_{H+He}$  main shock starts crossing the metal-poor photosphere at a lower optical depth with smaller  $Mach$  number.

(4) [Huete Ruiz de Lira \(2010\)](#) finds that shocks encountering the density inhomogeneities characteristic of convective envelopes generate turbulent velocities that dissipate shocks. We attribute the smaller Mach number of the main shock in metal-poor photosphere to their larger convective envelopes.

(5) Metal-poor atmospheres are very extended, particularly those of metal-poor type 2. In these stars the main shock propagates outwards into the upper extended atmosphere, and its amplitude increases with decreasing gas density, so it reaches higher Mach numbers in the upper atmosphere. A circumstellar envelope around the metal-poor RR ab type 2 may occur, perhaps as suggested recently by [Stellingwerf \(2013\)](#). These issues will be addressed in a subsequent paper.

Finally, we interpret the hydrodynamic gradient in metal-poor RRab, an abrupt hydrodynamic amplification process, as follows: in addition to the  $\kappa$  and  $\gamma$  mechanisms, metal-poor RR ab type 2 generate a third pulsation excitation mechanism, the radiation-modulated excitation mechanism, stronger than the  $\kappa$  and  $\gamma$  mechanisms that creates a new shock wave  $Sh_{RME}$  inducing a stronger main shock  $Sh_{H+He} + Sh_{RME}$  with higher Mach number and then an abrupt hydrodynamic amplification process. Indeed, such a pulsation excitation mechanism has been reported by [Xiong et al. \(1998\)](#) in the horizontal branch cooler convective envelopes with  $T_{eff} < 6200$  K which are similar to the metal-poor RR ab type 2 (Sect. 7.3) where the hydrodynamic gradient mechanism occurs. In fact, by the use of local time-dependant statistical theory of convection with a both the dynamic and thermodynamic coupling between convection and oscillations, [Xiong et al. \(1998\)](#) demonstrates that the radiation-modulated excitation mechanism depends on the gradient of the radiative luminosity (see equation 14 in [Xiong et al. \(1998\)](#)) and takes place in a zone of the radiation flux gradient which is the bottom and the top of the convective zone. This third process converts radiation energy into the kinetic energy of pulsation. We hypothesize that such radiation-modulated excitation could generate, in metal-poor RR ab type 2, a shock wave, that we call  $Sh_{RME}$ . This latter interferes with the  $\kappa$  and  $\gamma$  mechanisms shock  $Sh_{H+He}$  inducing a stronger resulting main shock ( $Sh_{H+He} + Sh_{RME}$ ) with an abrupt increase of  $Mach$  number and then the observed threshold effect in  $H\alpha$  emission that occurs near  $H\alpha$  radial velocity amplitude  $\sim 115$  km s $^{-1}$ . Further calculations are needed to clarify such synergies between hydrodynamic gradient and radiation-modulated excitation mechanisms.

We thank Jose Govea for initial analyses of some of the RR Lyr spectra. We are happy to acknowledge our referee for helpful comments that improved the manuscript. We thank all the Las Campanas Observatory support personnel for their help during the course of our endeavor, We offer our special regards to several duPont telescope operators for their efforts in assisting with the observations required to produce this paper. Finally, we are most grateful to Stephen Shetman for inventing the duPont echelle spectrograph thirty-some years ago. This work has been supported in part by NASA grant NNX10AN93G (J.E.L.), by NSF grant AST-1211055 (J.E.L.) and NSF grant AST-1211585 (C.S.).

## REFERENCES

- Arp, H. 1959, *AJ*, 64, 441
- Asplund, M., Grevesse, N., Sauval, A. J., & Scott, P. 2009, *ARA&A*, 47, 481
- Bailey, S. I. 1902, *Annals of Harvard College Observatory*, 38, 1
- Bellini, A., Piotto, G., Milone, A. P., et al. 2013, *ApJ*, 765, 32
- Bensby, T., Feltzing, S., & Oey, M. S. 2014, *A&A*, 562, A71
- Blanco, V. M. 1992, *AJ*, 104, 734
- Blazko, S. 1907, *Astronomische Nachrichten*, 175, 327
- Bono, G., Caputo, F., Cassisi, S., Castellani, V., & Marconi, M. 1997a, *ApJ*, 479, 279

- Bono, G., Caputo, F., Cassisi, S., Incerpi, R., & Marconi, M. 1997b, *ApJ*, 483, 811
- Brugamyer, E., Dodson-Robinson, S. E., Cochran, W. D., & Sneden, C. 2011, *ApJ*, 738, 97
- Carney, B. W., Storm, J., & Williams, C. 1993, *PASP*, 105, 294
- Chadid, M. 2000, *A&A*, 359, 991
- Chadid, M. 2011, in *RR Lyrae Stars, Metal-Poor Stars, and the Galaxy*, ed. A. McWilliam, 29
- Chadid, M., & Preston, G. W. 2013, *MNRAS*, 434, 552
- Chadid, M., Vernin, J., Preston, G., et al. 2014, *AJ*, 148, 88
- Clement, C. M., & Shelton, I. 1999, *ApJL*, 515, L85
- Clementini, G., Carretta, E., Gratton, R., et al. 1995, *AJ*, 110, 2319
- Corwin, T. M., Sumerel, A. N., Pritzl, B. J., et al. 2006, *AJ*, 132, 1014
- Cox, J. P. 1980, *Theory of stellar pulsation*
- de Boer, K. S., & Maintz, G. 2010, *A&A*, 520, A46
- Den Hartog, E. A., Ruffoni, M. P., Lawler, J. E., et al. 2014, *ApJS*, 215, 23
- Fernley, J., & Barnes, T. G. 1996, *A&A*, 312, 957
- For, B.-Q., Preston, G. W., & Sneden, C. 2011a, *ApJS*, 194, 38
- For, B.-Q., Sneden, C., & Preston, G. W. 2011b, *ApJS*, 197, 29
- Gallagher, A. J., Ryan, S. G., García Pérez, A. E., & Aoki, W. 2010, *A&A*, 523, A24
- Gillet, D., & Crowe, R. A. 1988, *A&A*, 199, 242
- Gilmore, G., & Reid, N. 1983, *MNRAS*, 202, 1025
- Govea, J., Gomez, T., Preston, G. W., & Sneden, C. 2014, *ApJ*, 782, 59
- Grevesse, N., Scott, P., Asplund, M., & Sauval, A. J. 2015, *A&A*, 573, A27
- Hansen, C. J., Nordström, B., Bonifacio, P., et al. 2011, *A&A*, 527, A65
- Huete Ruiz de Lira, C. 2010, *Physica Scripta Volume T*, 142, 014022
- Jurcsik, J. 1998, *A&A*, 333, 571
- Kolenberg, K., Fossati, L., Shulyak, D., et al. 2010, *A&A*, 519, A64
- Kollmeier, J. A., Szczygiel, D. M., Burns, C. R., et al. 2013, *ApJ*, 775, 57
- Kukarkin, B. V. 1949, in *Structure and Evolution of Stellar Systems*, Moscow: Government Printing Office, 182
- Kurucz, R. L. 2011, *Canadian Journal of Physics*, 89, 417
- Lambert, D. L., Heath, J. E., Lemke, M., & Drake, J. 1996, *ApJS*, 103, 183
- Lawler, J. E., Guzman, A., Wood, M. P., Sneden, C., & Cowan, J. J. 2013, *ApJS*, 205, 11
- Layden, A. C. 1994, *AJ*, 108, 1016
- . 1995a, *AJ*, 110, 2288
- . 1995b, *AJ*, 110, 2312
- Liu, S., Zhao, G., Chen, Y.-Q., Takeda, Y., & Honda, S. 2013, *Research in Astronomy and Astrophysics*, 13, 1307
- Marconi, M., Coppola, G., Bono, G., et al. 2015, *ApJ*, 808, 50
- McNamara, D. H. 1999, *PASP*, 111, 489
- Morrison, H. L., Flynn, C., & Freeman, K. C. 1990, *AJ*, 100, 1191
- Nemec, J. M., Cohen, J. G., Ripepi, V., et al. 2013, *ApJ*, 773, 181
- O'Brian, T. R., Wickliffe, M. E., Lawler, J. E., Whaling, W., & Brault, J. W. 1991, *Journal of the Optical Society of America B Optical Physics*, 8, 1185
- Pancino, E., Britavskiy, N., Romano, D., et al. 2015, *MNRAS*, 447, 2404
- Pojmanski, G. 2003, *AcA*, 53, 341
- Preston, G. W. 1959, *ApJ*, 130, 507
- . 2009, *A&A*, 507, 1621
- . 2011, *AJ*, 141, 6
- Preston, G. W., & Chadid, M. 2013, in *EAS Publications Series*, Vol. 63, *EAS Publications Series*, ed. G. Alecian, Y. Lebreton, O. Richard, & G. Vauclair, 35–45
- Preston, G. W., & Paczynski, B. 1964, *ApJ*, 140, 181
- Preston, G. W., Sheckman, S. A., & Beers, T. C. 1991, *ApJ*, 375, 121
- Preston, G. W., & Sneden, C. 2000, *AJ*, 120, 1014
- . 2001, *AJ*, 122, 1545
- Preston, G. W., Sneden, C., Thompson, I. B., Sheckman, S. A., & Burley, G. S. 2006, *AJ*, 132, 85
- Pritzl, B. J., Smith, H. A., Catelan, M., & Sweigart, A. V. 2002, *AJ*, 124, 949
- Reddy, B. E., Lambert, D. L., & Allende Prieto, C. 2006, *MNRAS*, 367, 1329
- Reddy, B. E., Tomkin, J., Lambert, D. L., & Allende Prieto, C. 2003, *MNRAS*, 340, 304
- Rich, R. M., Sosin, C., Djorgovski, S. G., et al. 1997, *ApJL*, 484, L25
- Roederer, I. U., Preston, G. W., Thompson, I. B., et al. 2014, *AJ*, 147, 136
- Roederer, I. U., Sneden, C., Thompson, I. B., Preston, G. W., & Sheckman, S. A. 2010, *ApJ*, 711, 573
- Ruchti, G. R., Fulbright, J. P., Wyse, R. F. G., et al. 2011, *ApJ*, 737, 9
- Samus, N. N., Kazarovets, E. V., Kireeva, N. N., Pastukhova, E. N., & Durlevich, O. V. 2010, *Odessa Astronomical Publications*, 23, 102
- Schmidt, E. G. 1991, *AJ*, 102, 1766
- Schwarzschild, M. 1952, in *Transactions of the IAU Vol. VIII*, ed. P. T. Oosterhoff, 811
- Scott, P., Asplund, M., Grevesse, N., Bergemann, M., & Sauval, A. J. 2015a, *A&A*, 573, A26
- Scott, P., Grevesse, N., Asplund, M., et al. 2015b, *A&A*, 573, A25
- Skarka, M. 2014, *MNRAS*, 445, 1584
- Sneden, C. 1973, *ApJ*, 184, 839
- Stellingwerf, R. F. 2013, *ArXiv e-prints*, arXiv:1310.0535
- Szczygiel, D. M., & Fabrycky, D. C. 2007, *MNRAS*, 377, 1263
- Taam, R. E., Kraft, R. P., & Suntzeff, N. 1976, *ApJ*, 207, 201
- Wallerstein, G., & Helfer, H. L. 1959, *ApJ*, 129, 720
- Wood, M. P., Lawler, J. E., Sneden, C., & Cowan, J. J. 2013, *ApJS*, 208, 27
- Xiong, D. R., Cheng, Q. L., & Deng, L. 1998, *ApJ*, 500, 449
- Zeldovich, Y. B., & Raizer, Y. P. 1966, *Elements of gasdynamics and the classical theory of shock waves*
- Zinn, R. 1985, *ApJ*, 293, 424

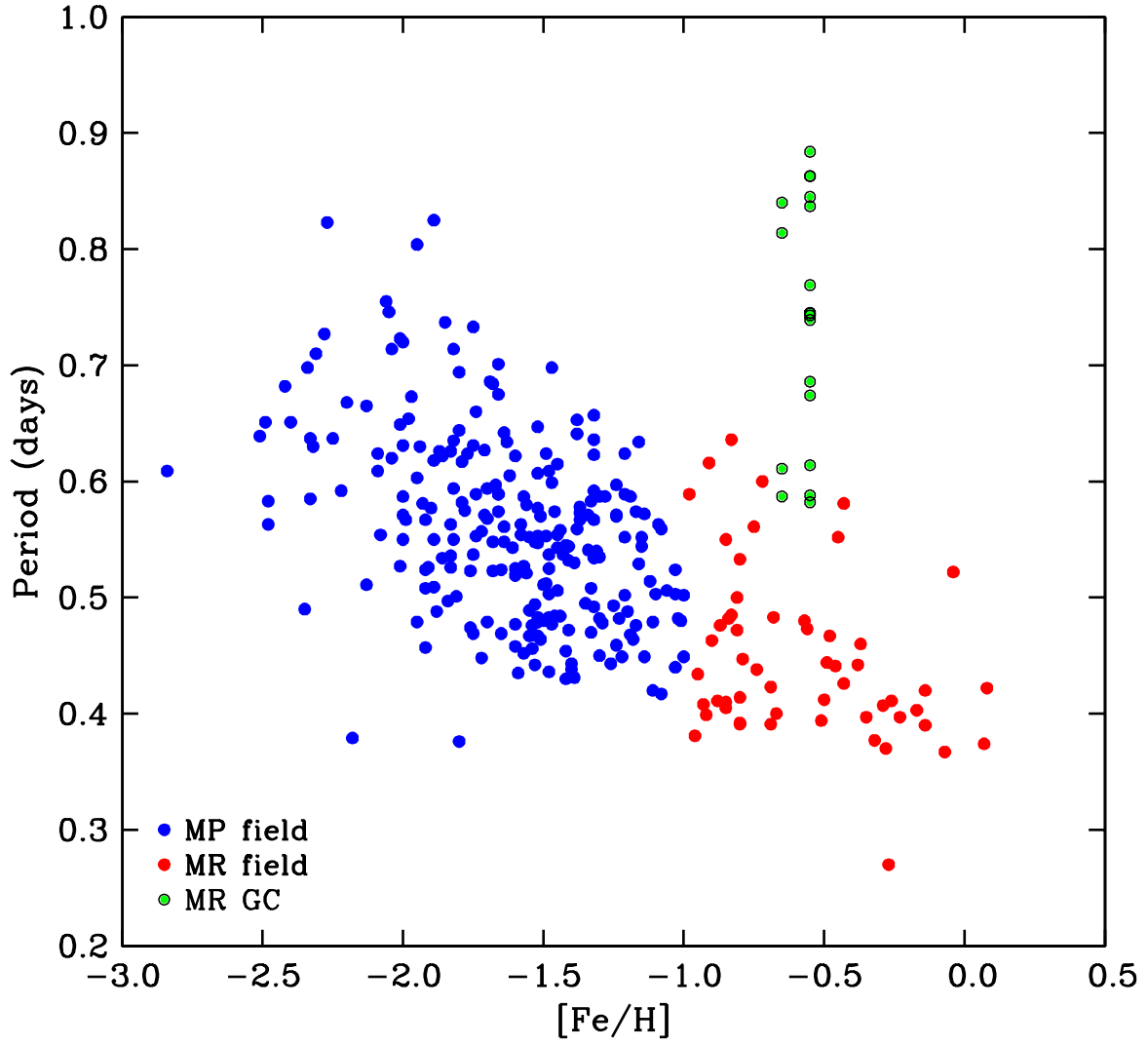


**Figure 1.** The pulsation periods of the RRab stars of Layden(1994) are plotted *versus* their  $[Fe/H]_{Lay94}$  values. This figure is adapted from Figure 1 of [Layden \(1995b\)](#).

As indicated in the figure legend, blue and red circles denote metal-poor (MP) and metal-rich (MR) stars, respectively. This symbol convention will be followed in all subsequent figures that divide stars into MP and MR categories. Green circles denote the RRab stars in NGC 6388 and NGC 6441.

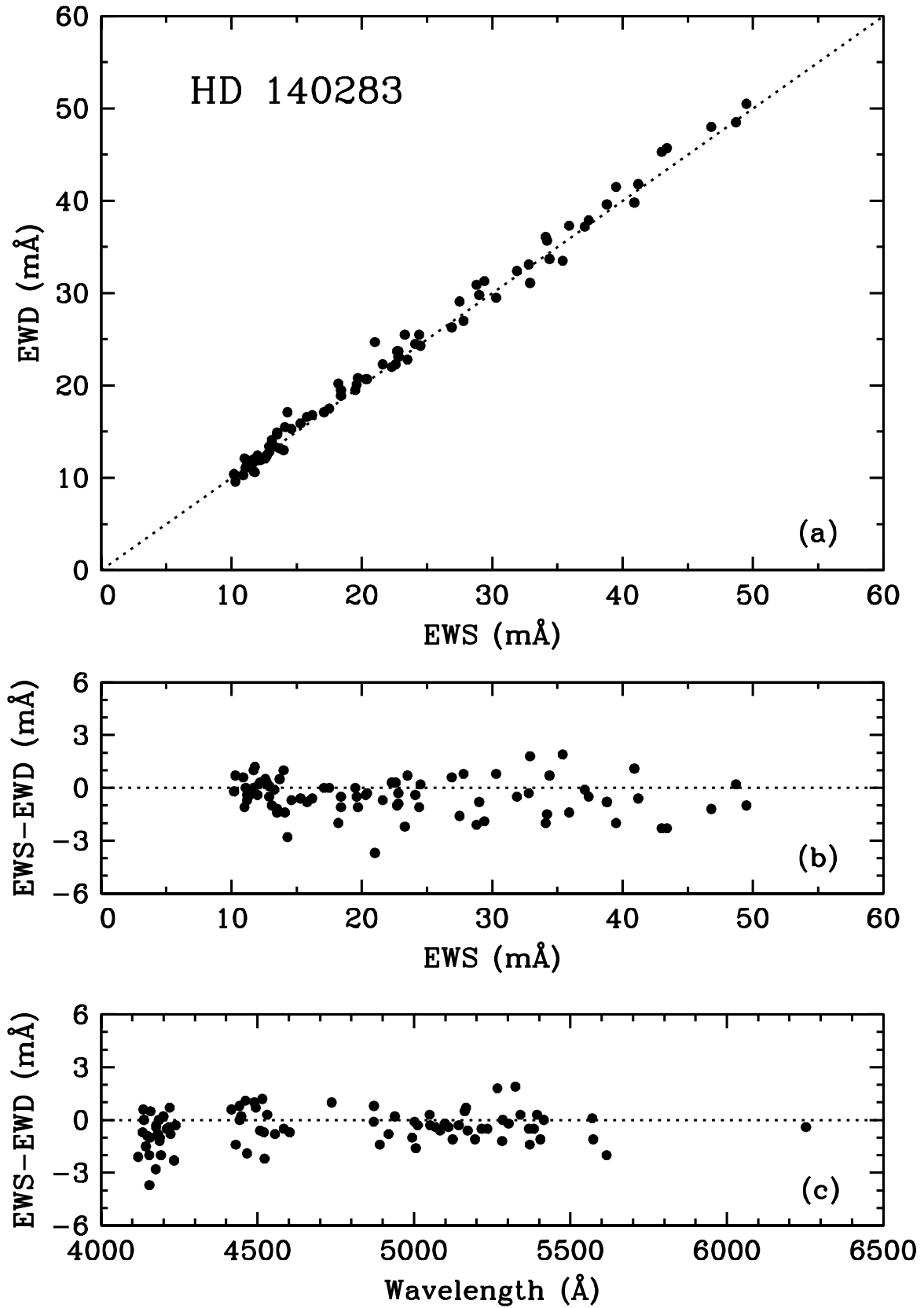


**Figure 2.** Equivalent widths HD 140283 Fe I and Fe II lines measured in du Pont spectra of (EWD) compared to the equivalent widths measured in a Subaru spectrum by [Gallagher et al. \(2010\)](#) (EWS). In panel (a) the two data sets are plotted against each other, and in panels (b) and (c) the EW differences are plotted *versus* EWS and wavelength, respectively

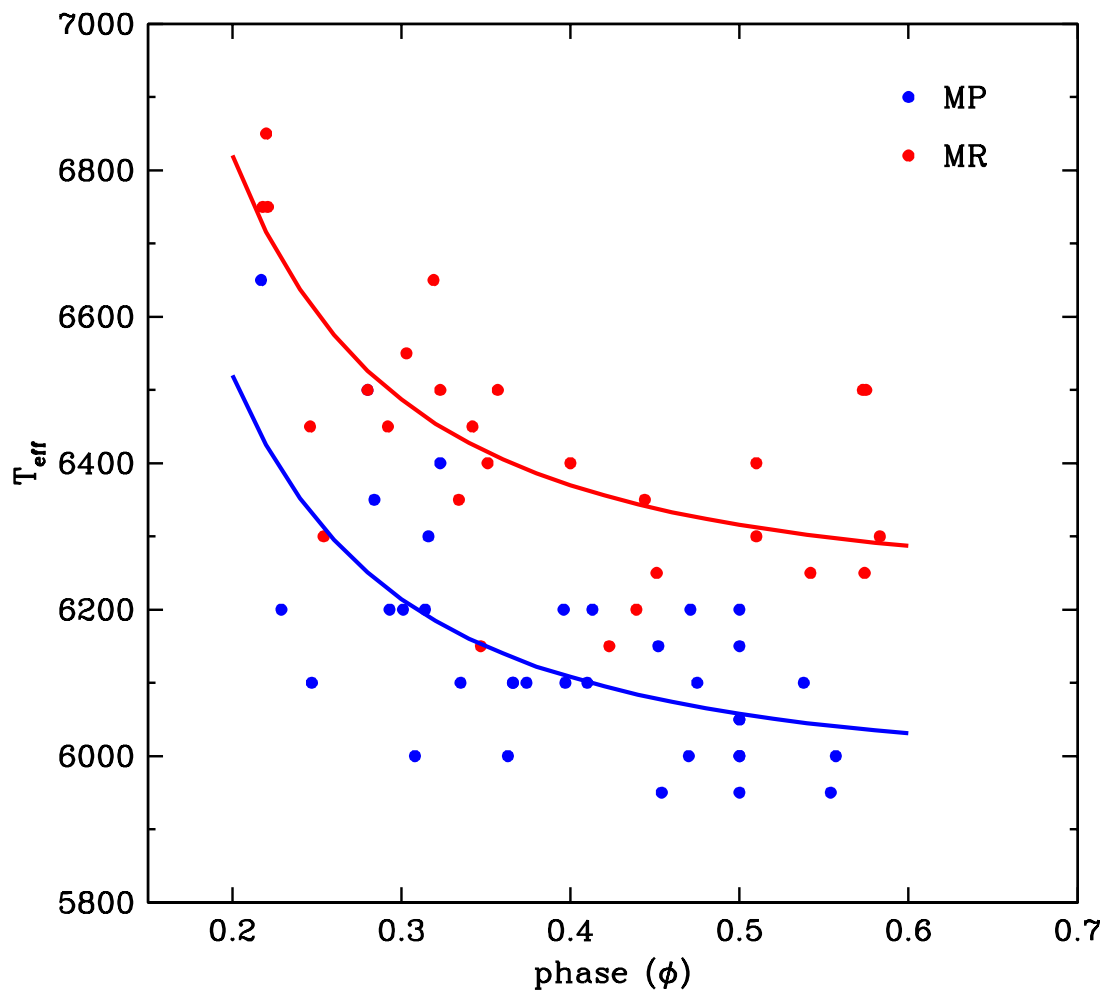


**Figure 3.** Correlations of derived  $T_{\text{eff}}$  values with pulsational phases  $\phi$  for metal-poor and metal-rich stars. The symbols are as in Figure 1. The curves are computed regression lines to the two metallicity populations.

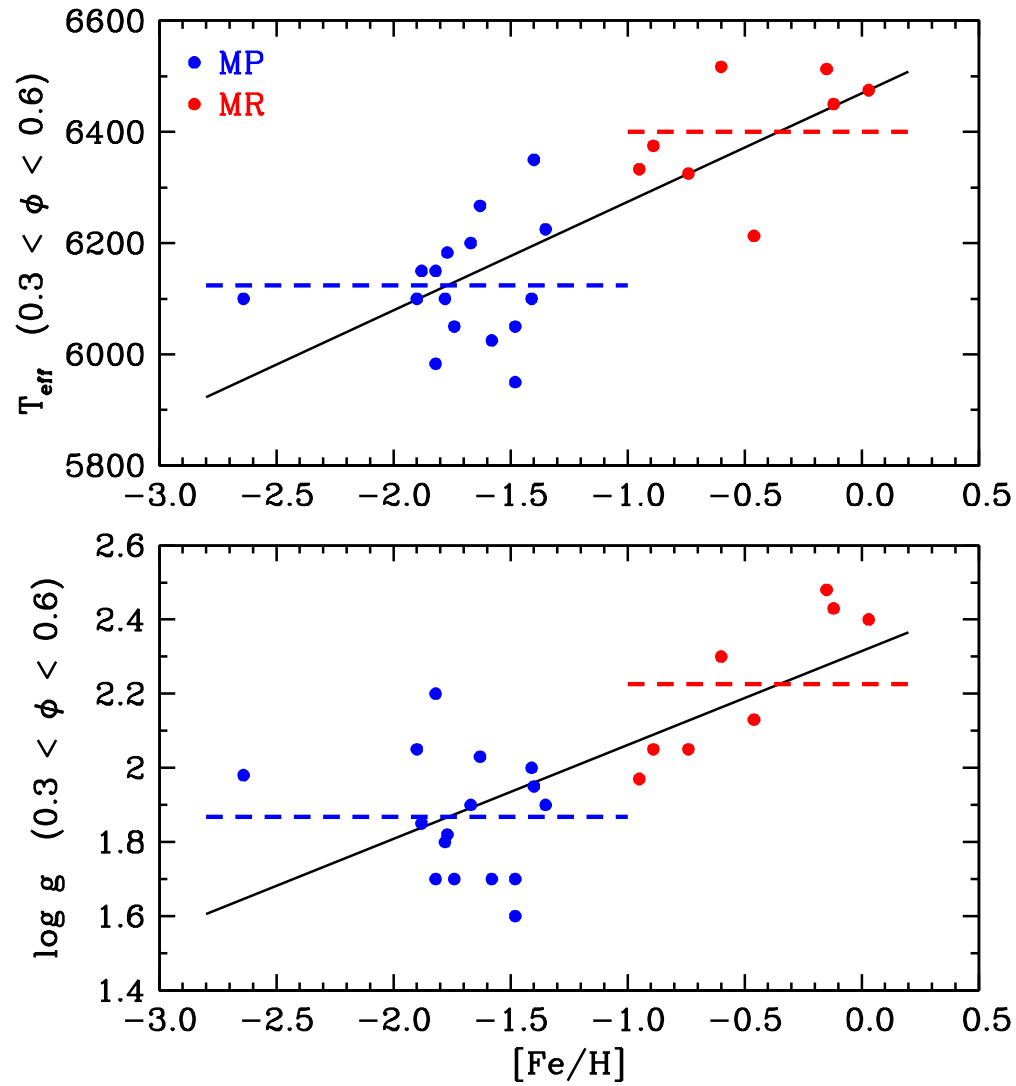


**Figure 4.** Temperatures (upper panel) and gravities (lower panel) of program stars plotted *versus* their metallicities. The symbols are as in Figure 1. Dashed horizontal lines in each panel depict the mean  $T_{\text{eff}}$  and  $\log g$  values of metal-rich and metal-poor stars. The solid black lines represent linear regression fits to all the data points.

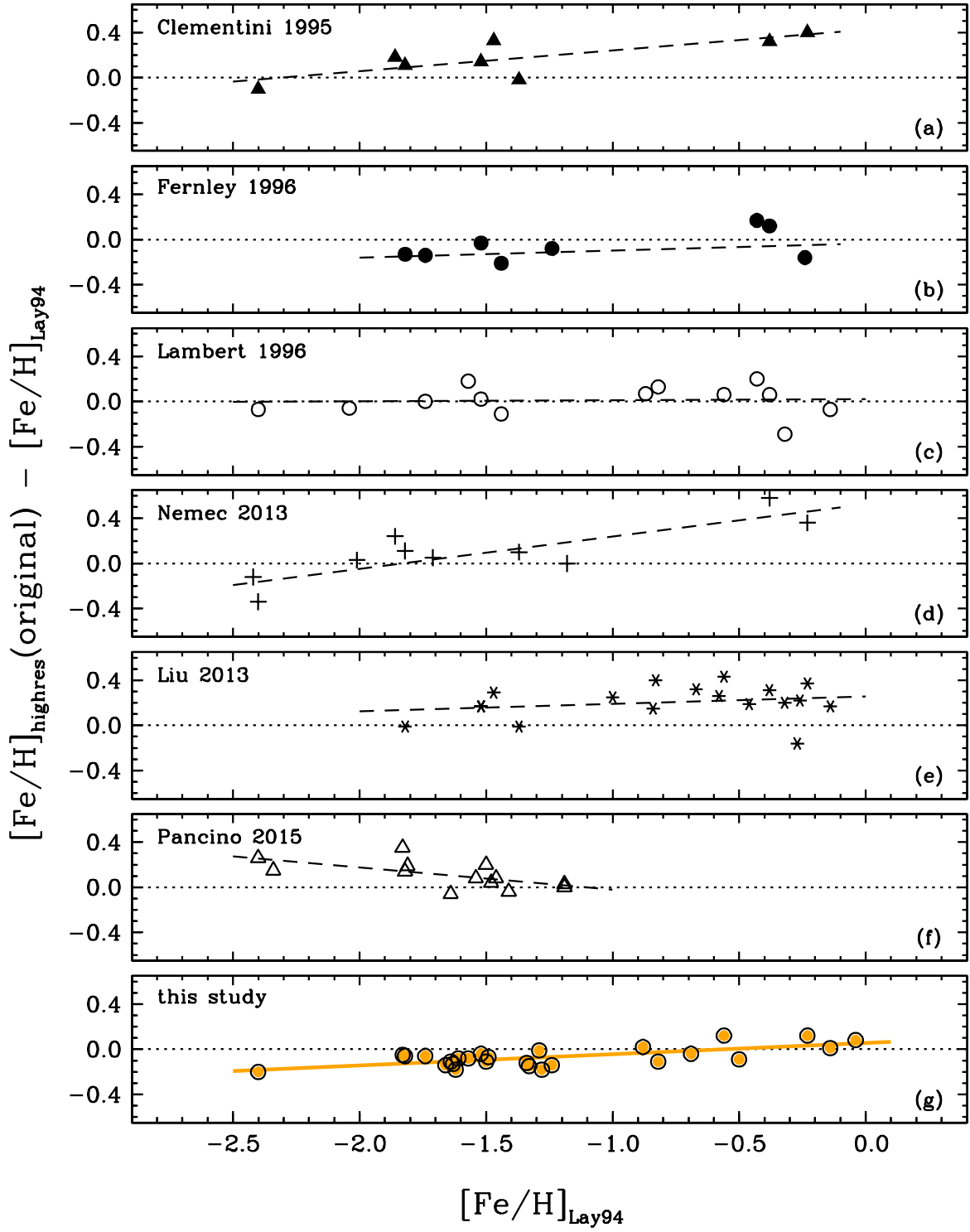


**Figure 5.** Differences between RR Lyr  $[\text{Fe}/\text{H}]$  “original” metallicities reported in seven high-resolution spectroscopic studies and those derived by Lay9 from calibrated  $\Delta S$  indices, plotted as functions of the Lay94 values. The symbols used in this figure to distinguish among the different studies will be also used in Figures 6 and 7. Sources briefly named in the figure panels are: (a), [Clementini et al. \(1995\)](#), (b) [Fernley & Barnes \(1996\)](#), (c) [Lambert et al. \(1996\)](#), (d) [Nemec et al. \(2013\)](#), (e) [Liu et al. \(2013\)](#), (f) [Pancino et al. \(2015\)](#), and (g) this study. The orange line in the bottom panel represents a linear regression fit to the metallicities derived here.

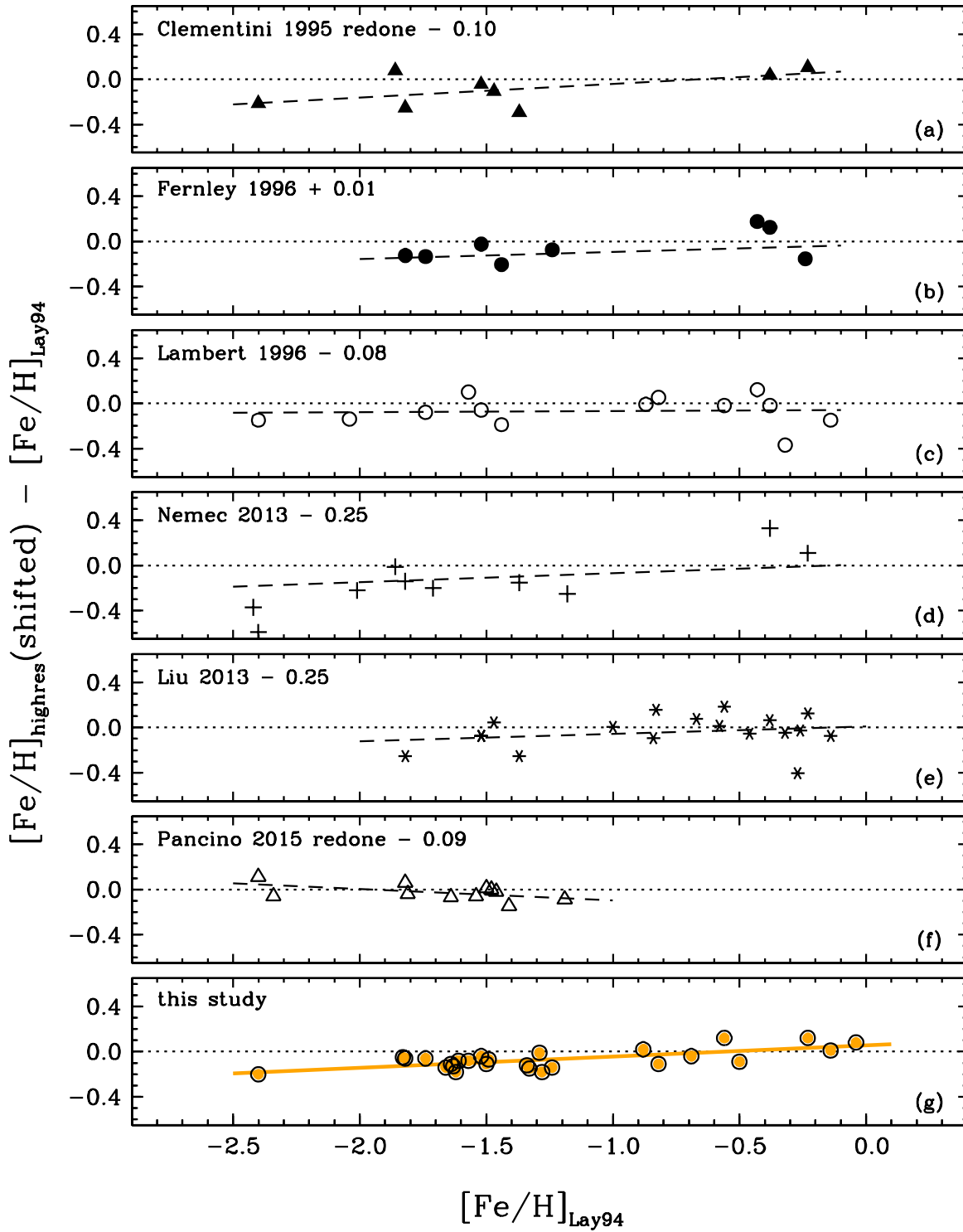


**Figure 6.** Another comparison between high-resolution spectroscopic metallicities and the Lay94  $\Delta S$  metallicities, but after reanalysis of the *EWs* of Clementini et al. (1995) and Pancino et al. (2015), and application of additive constants to bring agreement between the literature results and those of this study at  $[\text{Fe}/\text{H}] = -1.25$ . See the text for details of this procedure. The symbols are as in Figure 5.

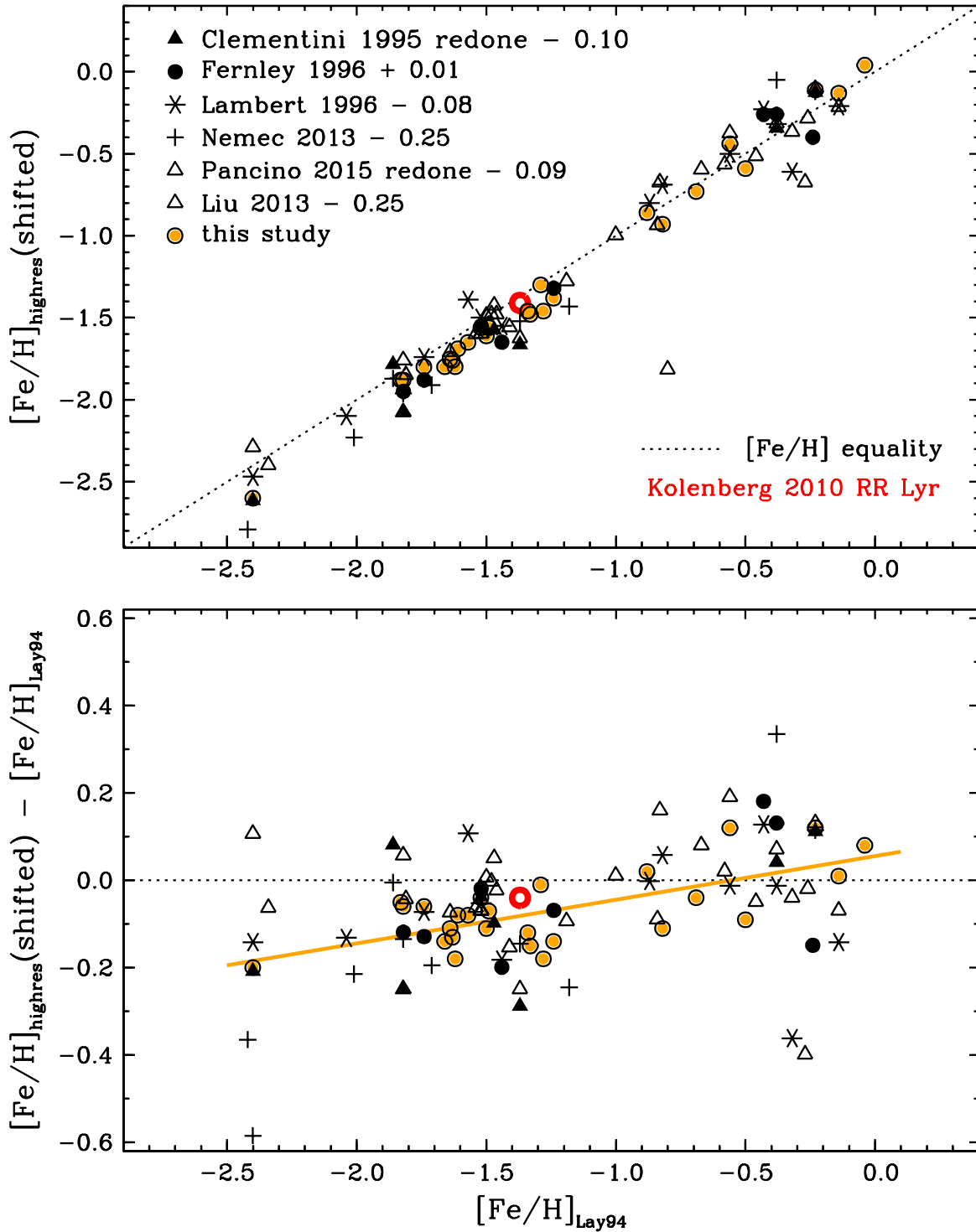


**Figure 7.** Final comparison between high-resolution spectroscopic metallicities and those of Lay94, after the reanalyses and scale shifts as described in the text have been applied. Symbols (consistent with those of Figure 5) are redefined in the upper panel. A red circle has been added to denote the metallicity for the star RR Lyr that was derived by Kolenberg et al. (2010).

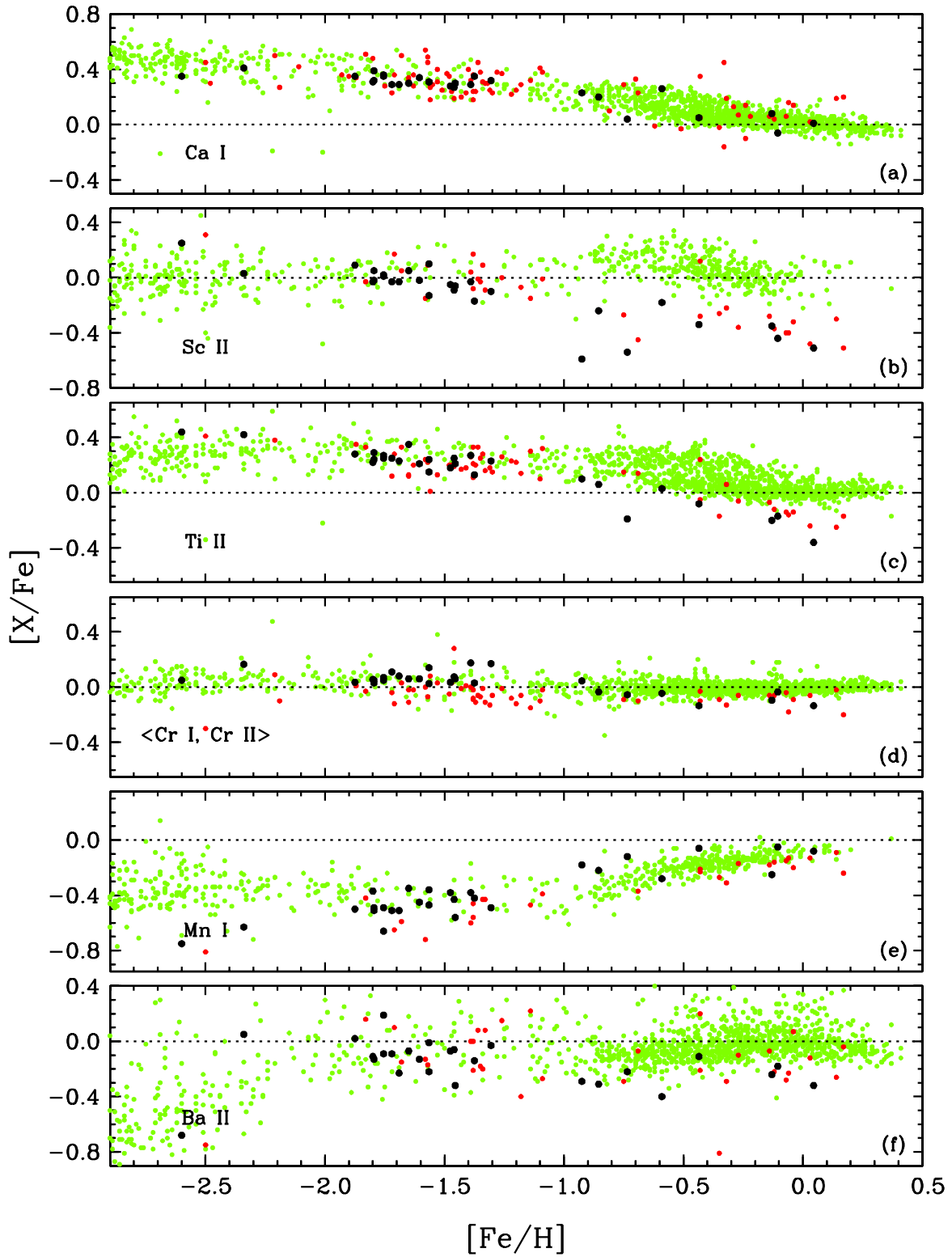


**Figure 8.** Relative abundance ratios as functions of  $[Fe/H]$  metallicity from our study (black dots), other RR Lyr publications (red dots), and from several very large-sample abundance surveys of non-variable main sequence, subgiant, and red giant stars. See text for sources of the external data.

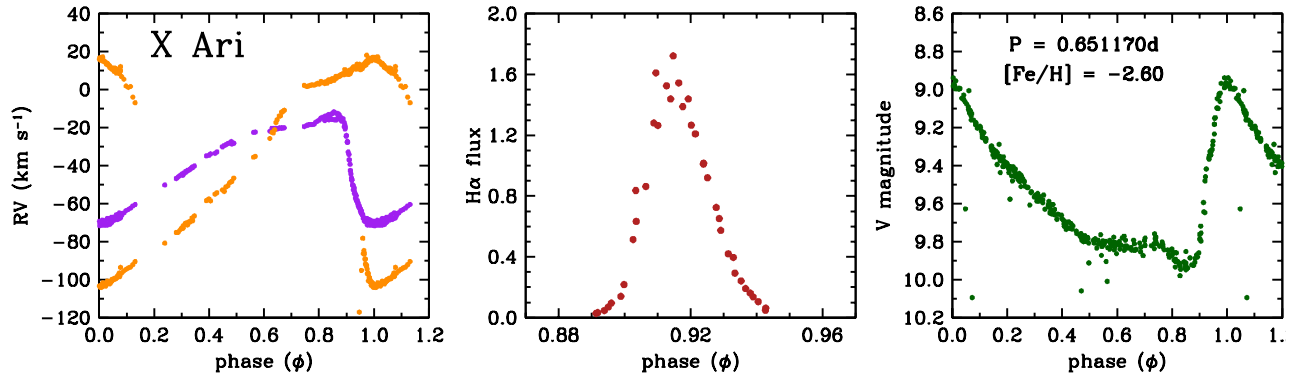


**Figure 9.** Variations in metallic-line (purple points) and  $\text{H}\alpha$  (orange points) radial velocities (left panel),  $\text{H}\alpha$  emission (middle panel), and V-band magnitude as functions of pulsational phase. Only the data for X Ari are shown here; the plots for the other 23 non-Blažhko program stars are available in the on-line version of this paper.

**Fig. Set 9. Velocities, Halpha Fluxes, and V Magnitudes for the Program Stars**

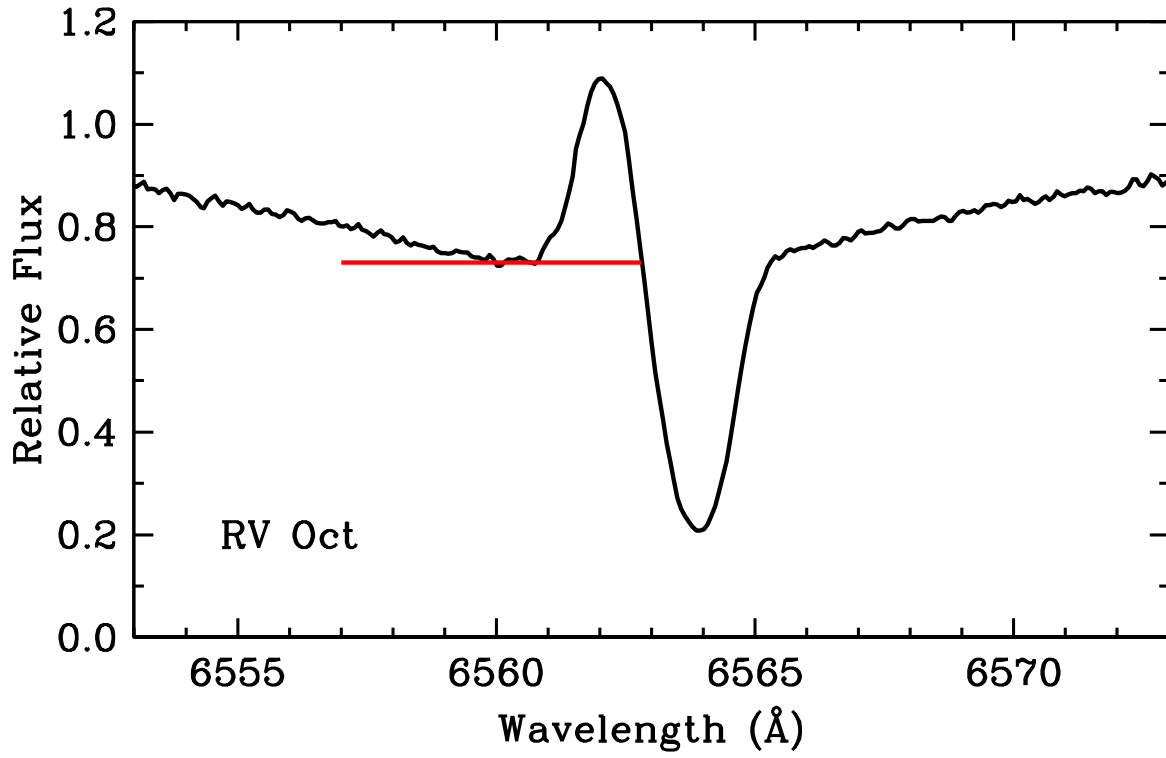


**Figure 10.** H $\alpha$  emission flux at phase  $\phi = 0.943$  in RV Oct is measured as the sum of flux counts above the reference level indicated by the horizontal red line.

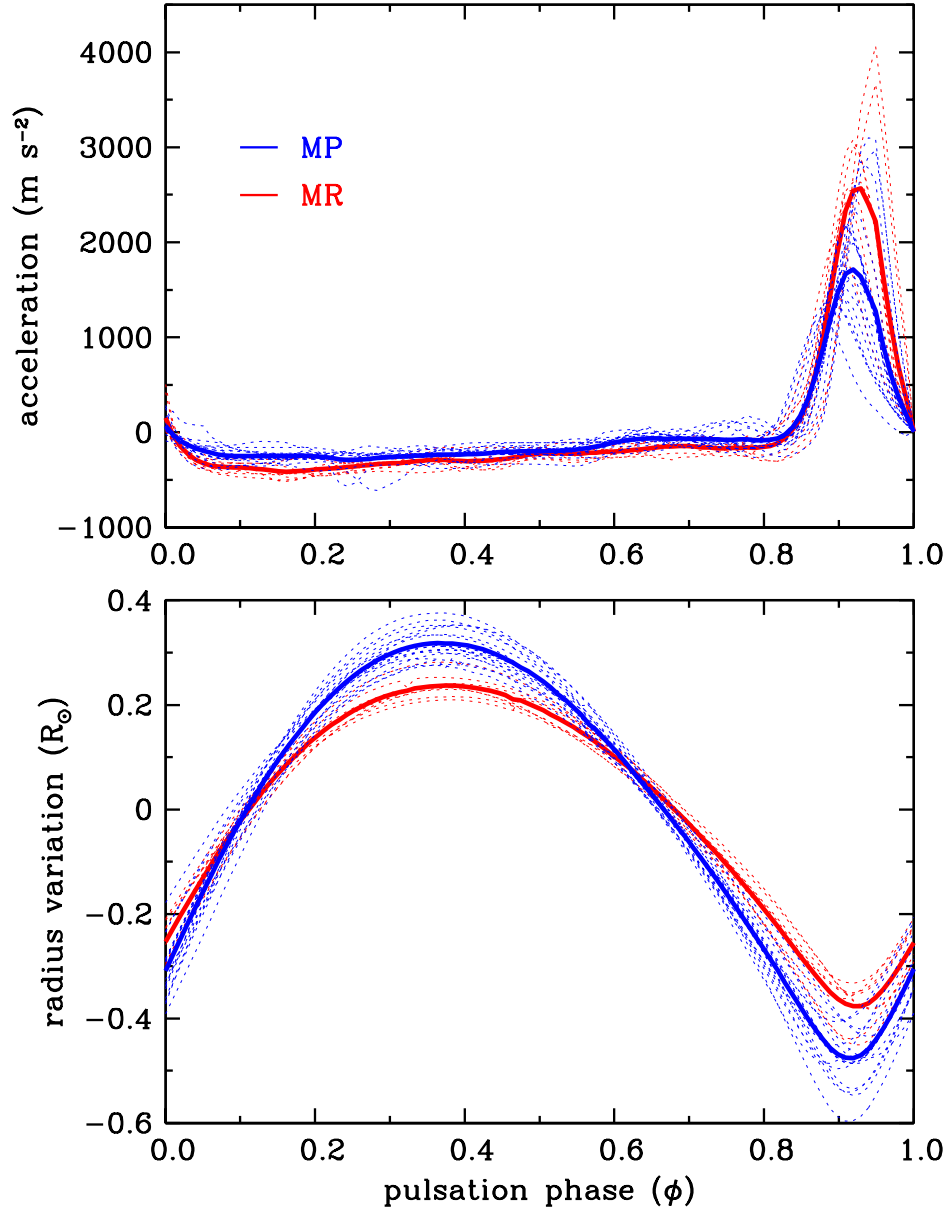


**Figure 11.** Dynamical acceleration and radius variation curves for metal-rich RR ab stars (MR; red lines) and metal-poor RR ab stars (MP; blue lines). The thin dashed lines show the accelerations and radius variations for individual stars, and the thick solid lines are for simple means constructed of the MR and MP data.

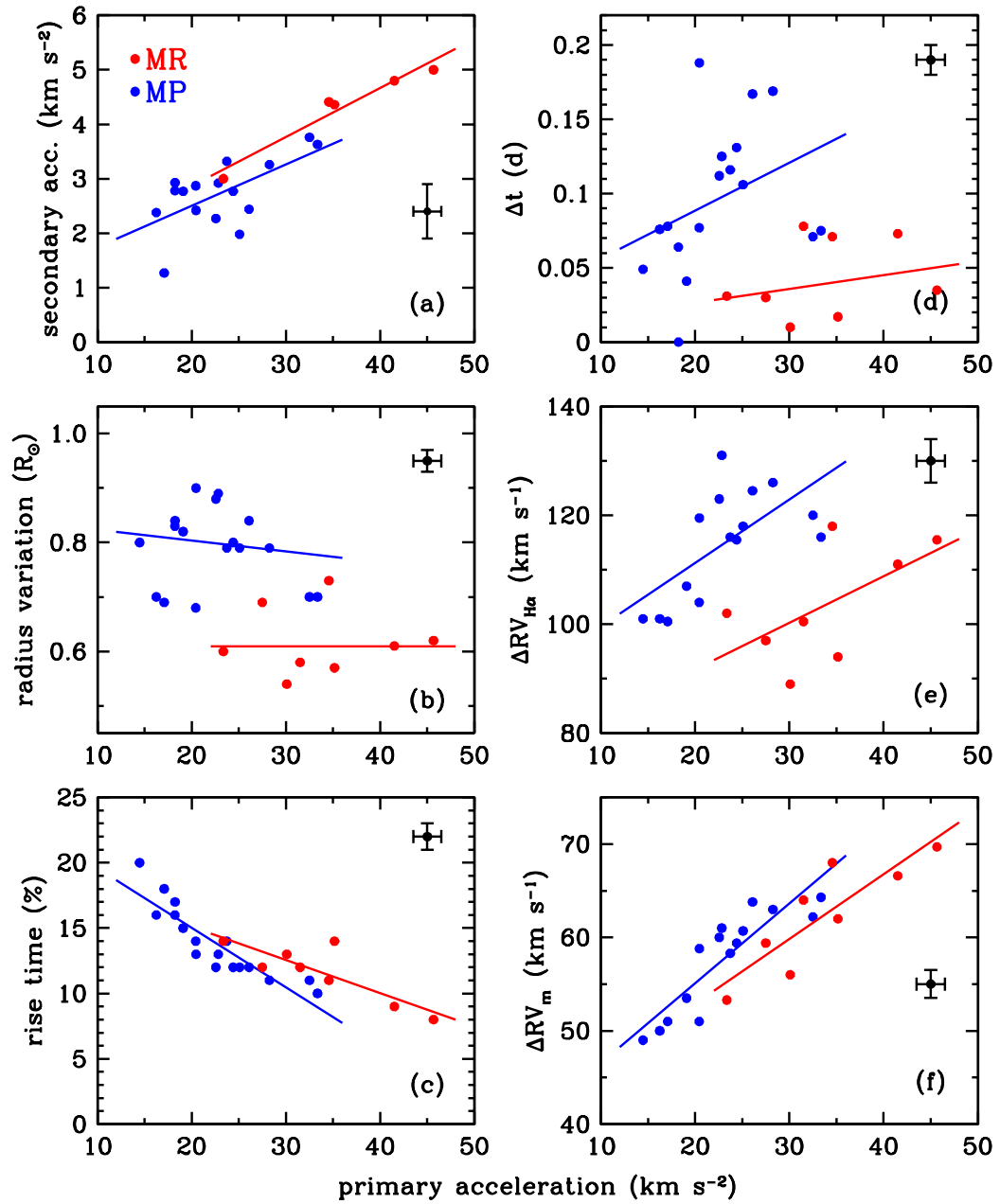


**Figure 12.** Secondary acceleration, radius variation, rise time, duration of H $\alpha$  doubling, H $\alpha$  RV amplitude and metal RV amplitude *versus* primary acceleration for metal-poor (blue) and metal-rich (red) RRab stars. Uncertainty estimates for the quantities are plotted in the figure captions; see Table 6.

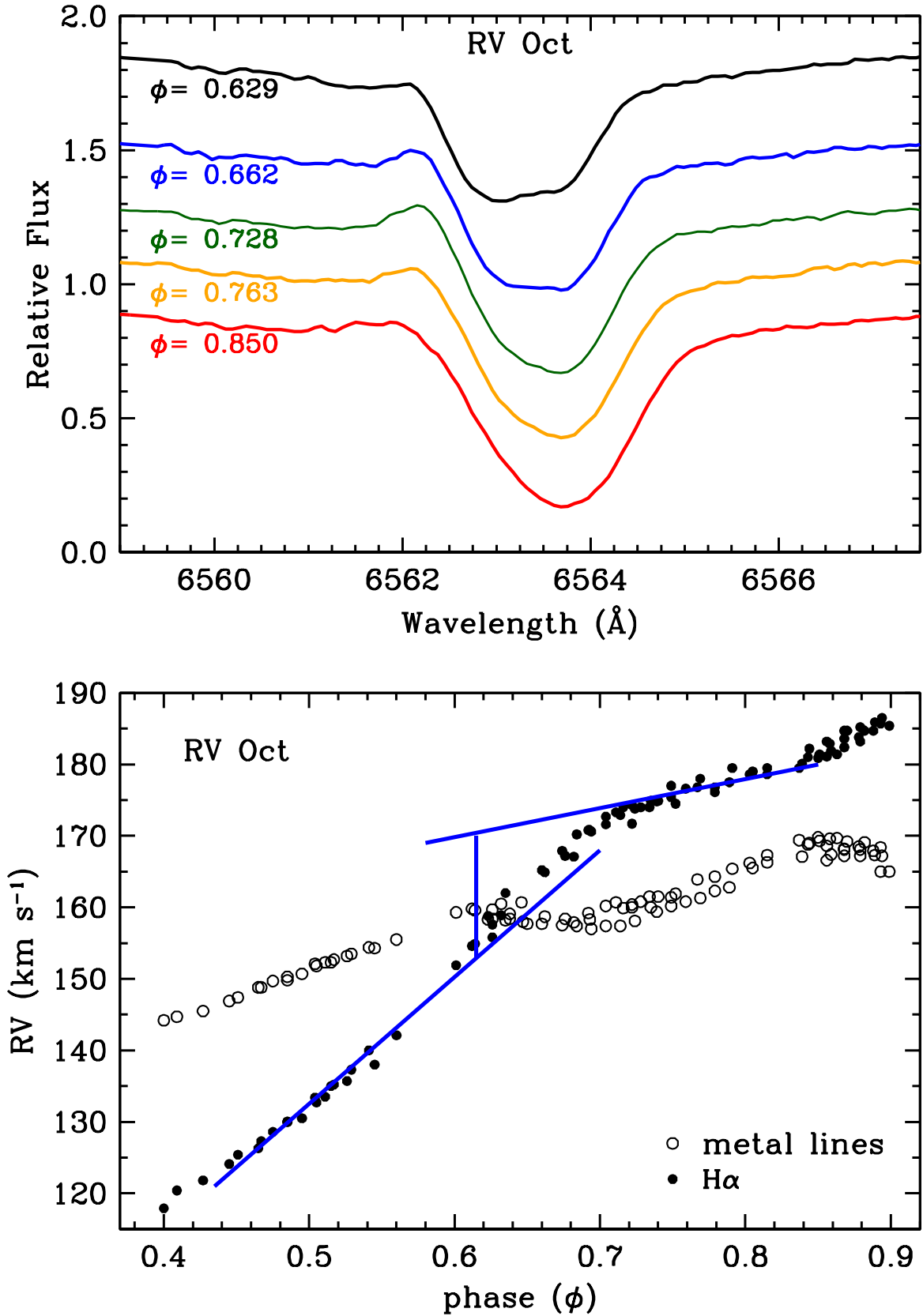


**Figure 13.** The top panel contains a sequence of H $\alpha$  profiles during the  $Sh_{PM3}$  shock in the phase interval  $0.63 < \phi < 0.85$ . The bottom panel shows metal (open black) and H $\alpha$  (solid black) radial velocities in this phase interval. The blue vertical line marks a  $20 \text{ km s}^{-1}$  shock discontinuity in H $\alpha$  radial velocity, evident in the line profiles at left.

## Bump line-doubling mechanism

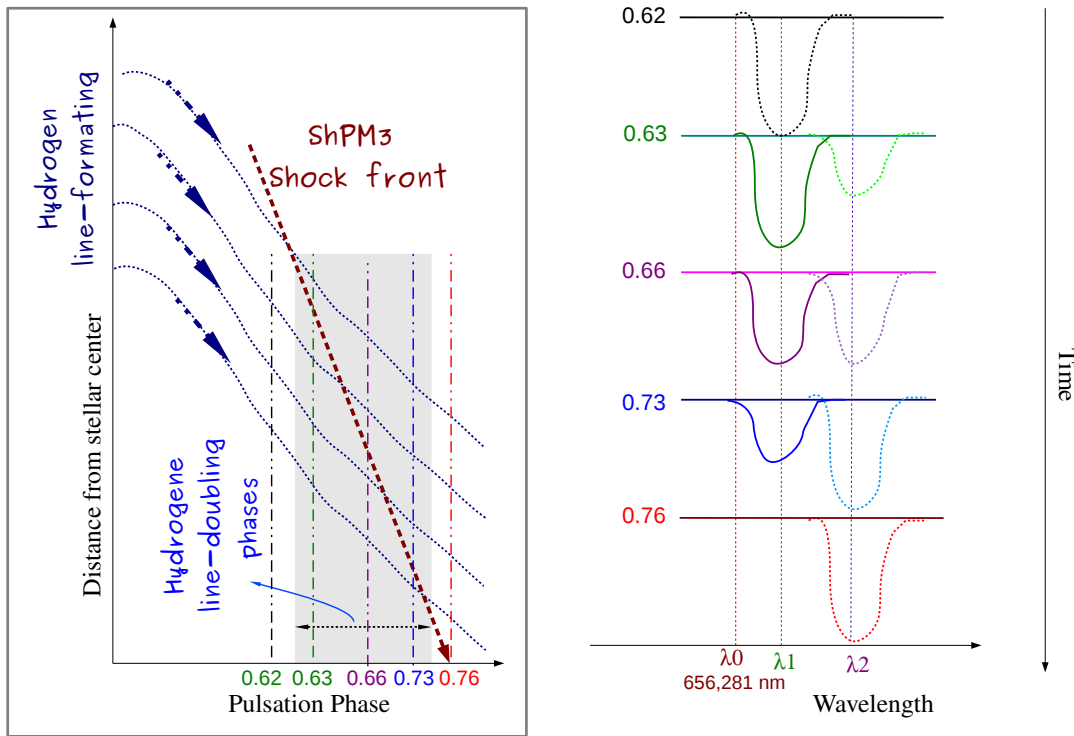


**Figure 14.** Bump line-doubling mechanism: temporal sequence followed by the intensity of both red components of H $\alpha$  line-doubling during the bump in the light curve, close to the light minimum, when the  $Sh_{PM3}$  ballistic shock wave propagates through the inward motion photosphere without the presence of any complicated radiative process due to the shock wave. We assume in this line-doubling mechanism that the four layers have an inward motion with a quasi-equal velocity towards the center of the star. An inward shock appears, with a greater velocity, progressively gets across the layers and changes their velocity to an higher velocity, inducing a small red-shifted component that gradually increases when the shock deeply gets through the layers.

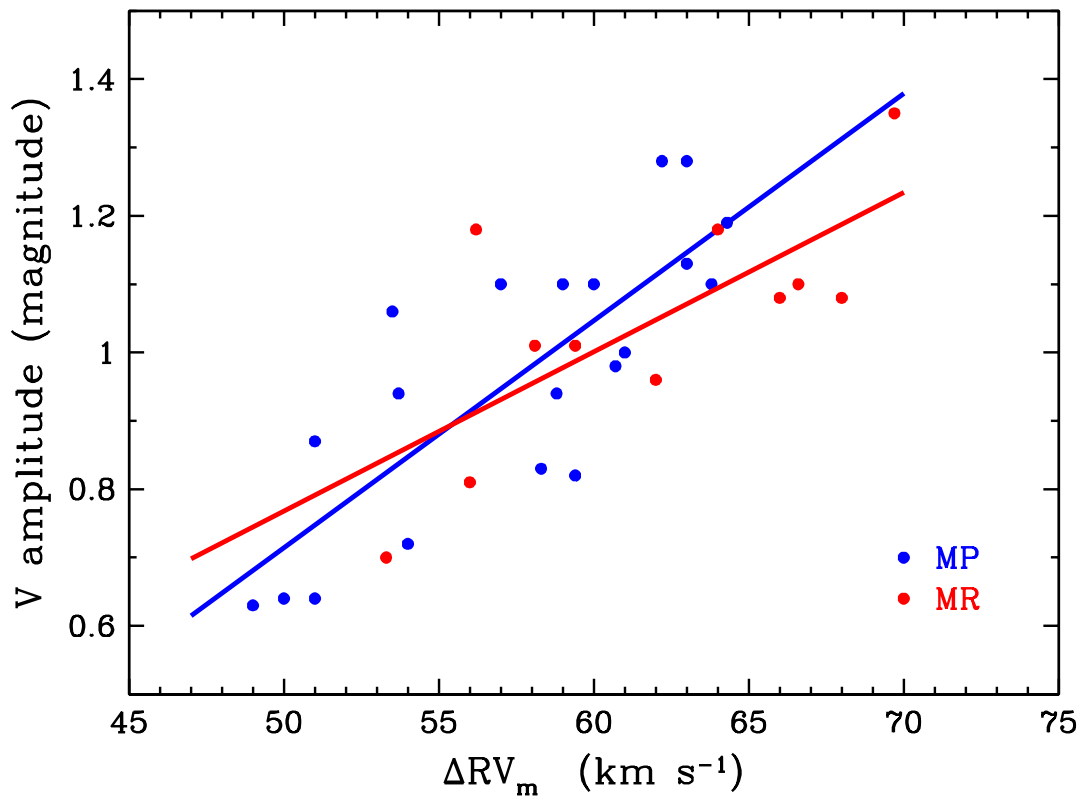


**Figure 15.** The correlations between  $V$  light amplitude and metallic line (photospheric) radial velocity amplitude for metal-poor (blue) and metal-rich (red) RRab stars.

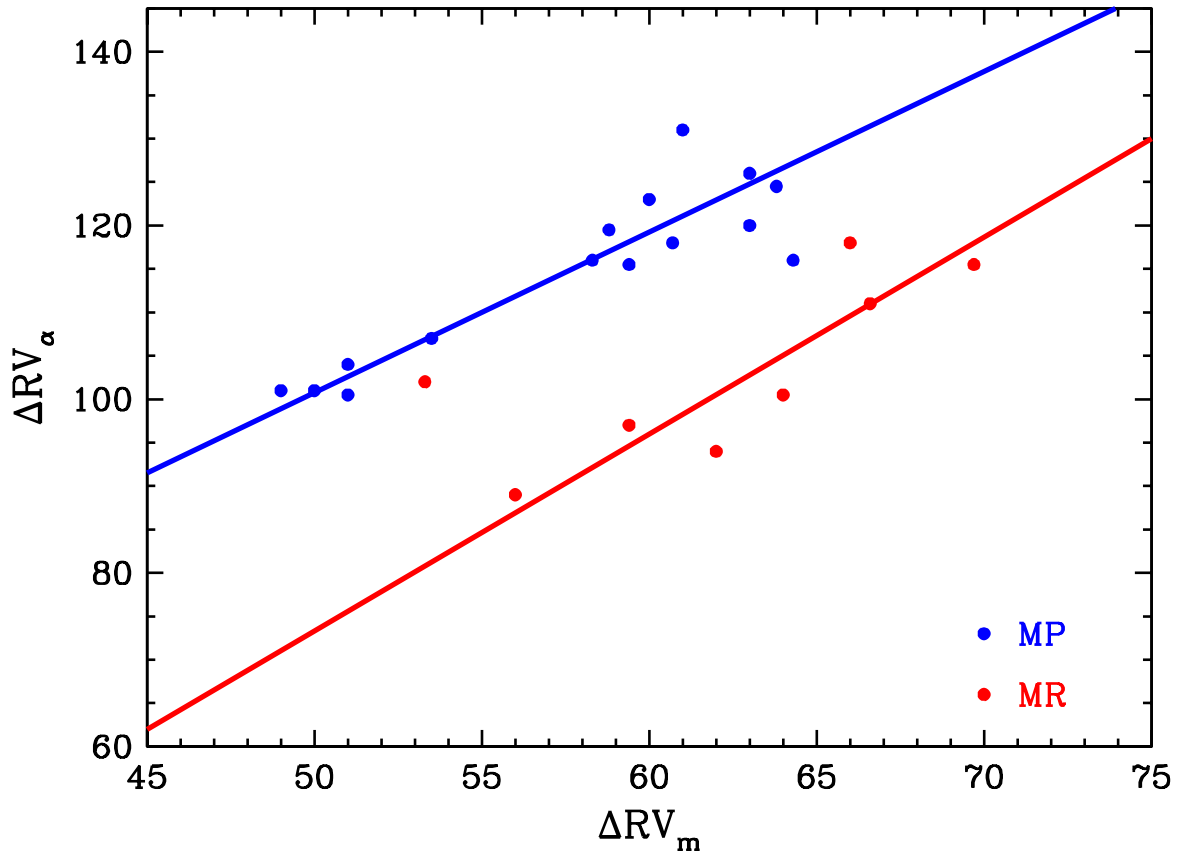
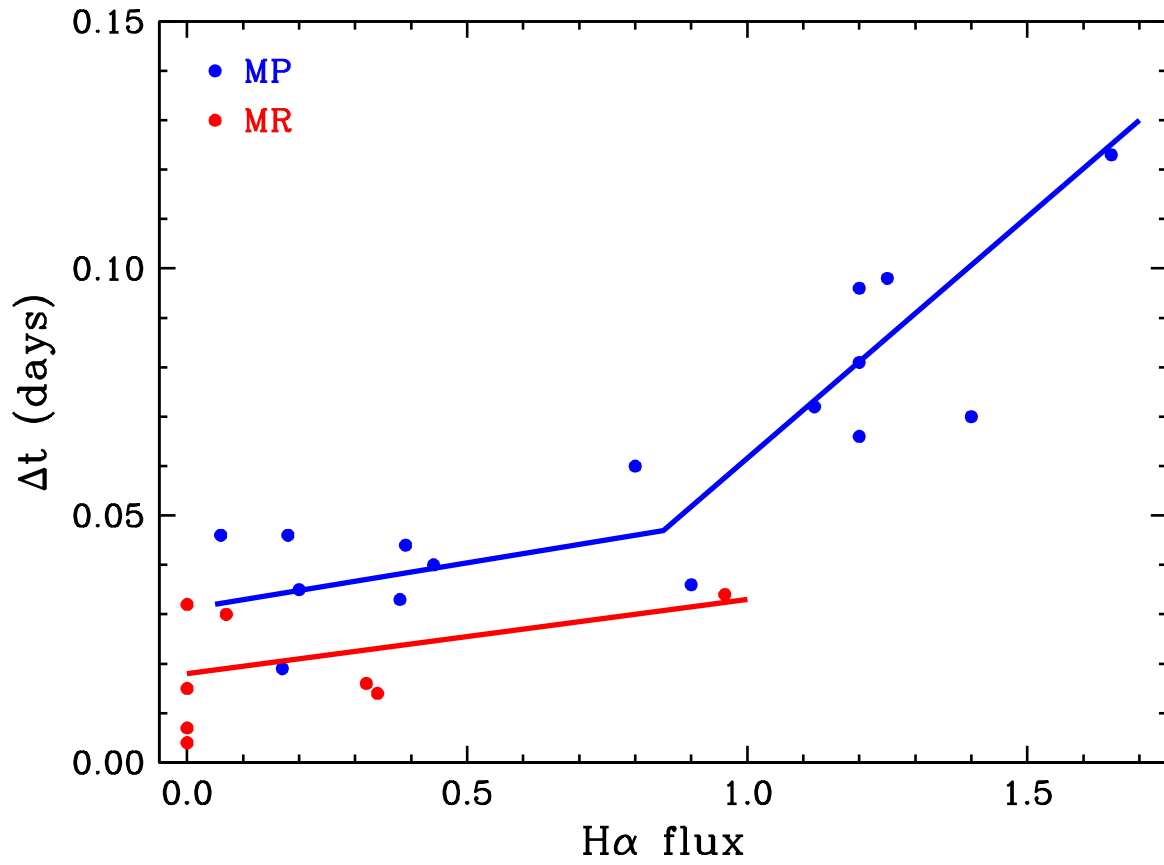


Figure 16. A plot of H $\alpha$  RV amplitude *versus* metal RV amplitude for metal-poor (blue) and metal-rich (red) RRab stars.



**Figure 17.** Duration of H $\alpha$  doubling *versus* H $\alpha$  peak flux for metal-poor (blue) and metal-rich (red) RRab stars. H $\alpha$  flux is measured in units of the normalized continuum flux at 6500 Å.

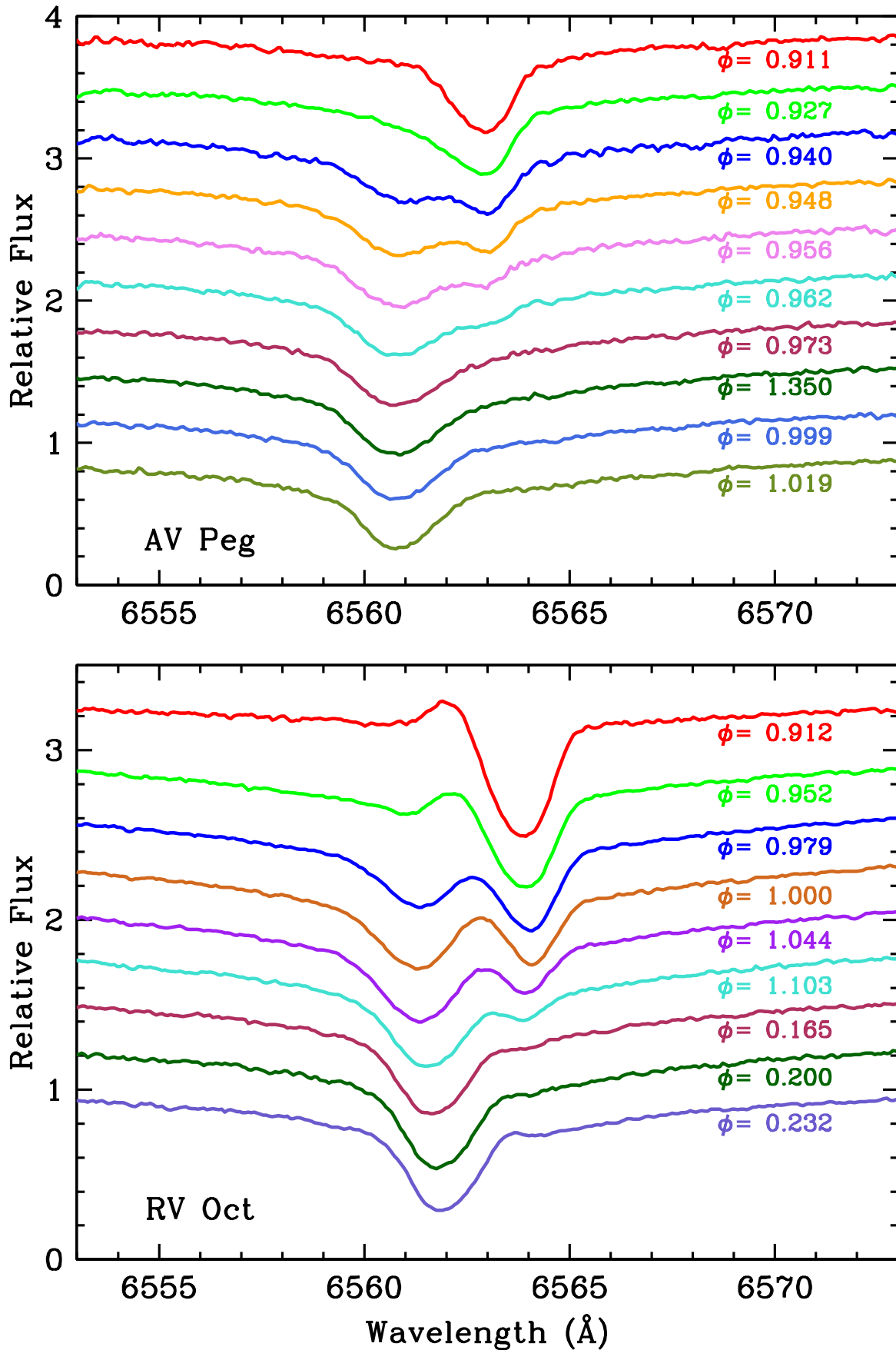
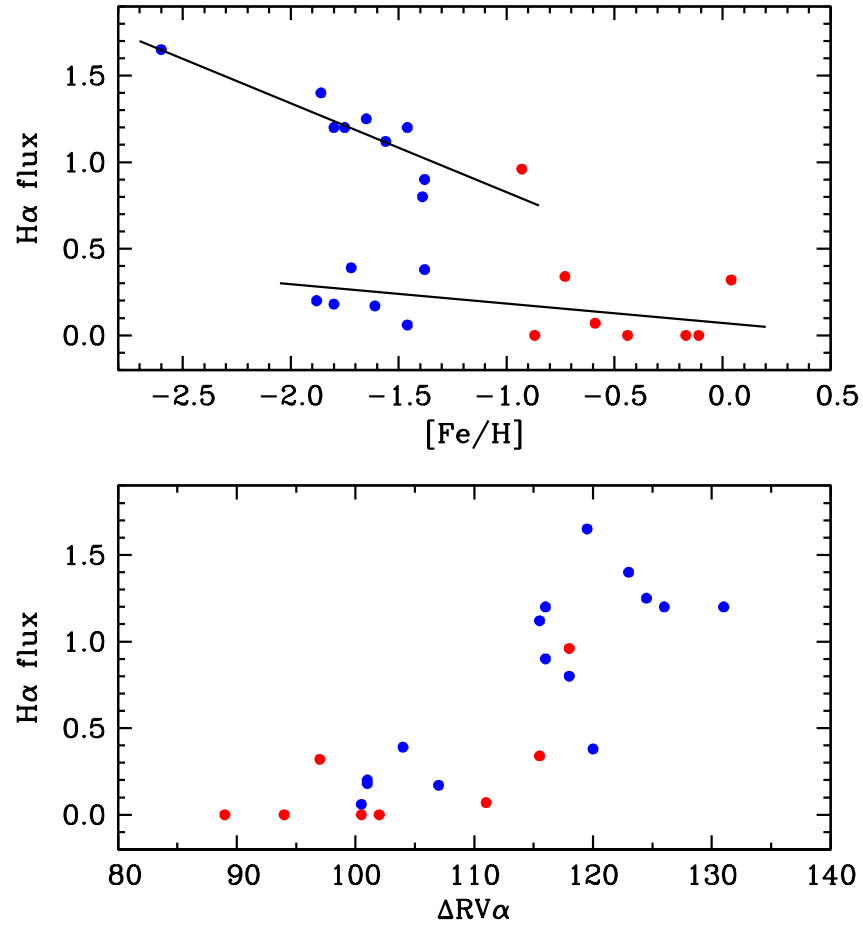


Figure 18. Spectra of the H $\alpha$  line profile as selected phases of metal-rich AV Peg (top panel) and metal-poor RV Oct (bottom panel).



**Figure 19.**  $H\alpha$  emission as function of metallicity (top panel) and hydrogen radial velocity amplitude (bottom panel).  $H\alpha$  flux is measured in units of the normalized continuum flux at 6500 Å.

**Table 1.** Program Star Data

Name GCVS	Name ASAS <sup>a</sup>	RA <sub>2000</sub> ASAS	Dec <sub>2000</sub> ASAS	<i>P</i> ASAS	<i>T</i> <sub>0</sub> ASAS	<i>V</i>	<i>V</i> <sub>amp</sub>	[Fe/H] Lay94 <sup>b</sup>
WY Ant	101605-2943.7	10:16:05	-29:43:42	0.574340	1870.76	10.37	0.85	-1.66
BS Aps	162051-7140.3	16:20:51	-71:40:18	0.582577	1915.69	11.90	0.68	-1.33
XZ Aps	145205-7940.7	14:52:05	-79:40:42	0.587300	1887.15	11.94	1.10	-1.57
DN Aqr	231917-2413.0	23:19:17	-24:13:00	0.633758	1872.33	10.85	0.72	-1.63
SW Aqr	211518+0004.6	21:15:18	0:04:36	0.459300	1876.17	10.56	1.28	-1.24
X Ari	030831+1026.8	3:08:31	10:26:48	0.651172	1890.10	9.24	0.94	-2.40
RR Cet	013208+0120.5	1:32:08	1:20:30	0.553030	2143.63	9.26	0.82	-1.52
W Crt	112630-1754.9	11:26:30	-17:54:54	0.412011	1871.64	10.90	1.10	-0.50
DX Del	204729+1227.8	20:47:29	12:27:48	0.472650	2415.85	9.81	0.70	-0.56
SX For	033022-3603.2	3:30:22	-36:03:12	0.605350	1870.42	10.89	0.64	-1.62
DT Hya	115400-3115.7	11:54:00	-31:15:42	0.567970	1872.11	12.53	0.98	...
V Ind	211130-4504.5	21:11:30	-45:04:30	0.479600	1873.49	9.62	1.06	-1.50
SS Leo	113355-0002.0	11:33:55	-00:02:00	0.626330	1873.06	10.47	1.00	-1.83
ST Leo	113833+1033.7	11:38:33	10:33:42	0.477983	2384.94	10.99	1.19	-1.29
Z Mic	211623-3017.0	21:16:23	-30:17:00	0.586930	1873.36	11.32	0.64	-1.28
RV Oct	134632-8424.1	13:46:32	-84:24:06	0.571184	1891.66	10.53	1.13	-1.34
UV Oct	163225-8354.2	16:32:25	-83:54:12	0.542561	1890.60	9.19	0.82	-1.61
V0445 Oph	162441-0632.5	16:24:41	-06:32:30	0.397030	1939.03	10.54	0.81	-0.23
AV Peg	215203+2234.4	21:52:03	22:34:24	0.390385	2758.11	9.95	0.96	-0.14
HH Pup	072036-4642.5	7:20:36	-46:42:30	0.390745	1869.65	10.57	1.24	-0.69
AN Ser	155331+1257.6	15:53:31	12:57:36	0.522080	2701.17	10.46	1.01	-0.04
VY Ser	153102+0141.0	15:31:02	1:41:00	0.714100	1922.71	9.84	0.63	-1.82
v1645 Sgr	202044-4107.1	20:20:44	-41:07:06	0.552979	1876.53	10.99	0.84	-1.74
W Tuc	005810-6323.8	0:58:10	-63:23:48	0.642260	1869.52	10.90	1.11	-1.64
CD Vel	094438-4552.6	9:44:38	-45:52:36	0.573510	1869.91	11.66	0.87	...
AS Vir	125246-1015.6	12:52:46	-10:15:36	0.553439	1886.61	11.66	0.72	-1.49
ST Vir	142739-0054.1	14:27:39	-00:54:06	0.410806	1906.92	11.00	1.18	-0.88
UU Vir	120835-0027.4	12:08:35	-00:27:24	0.475597	1886.54	10.06	1.08	-0.82

<sup>a</sup> All Sky Automated Survey (Pojmanski 2003)<sup>b</sup> Lay94

**Table 2.** Standard deviations of the regressions

Quantity	MP	MR	ALL
$T_{\text{eff}}$	102	100	108
$\log g$	0.16	0.19	0.18

**Table 3.** Model Atmosphere Parameters

Star	[Fe/H]	$\phi$	$T_{\text{eff}}$	$\log g$	$\xi_t$	[M/H]	[Fe/H]	$\sigma$	#	[Fe/H]	$\sigma$	#
	Lay94		K			model	I			I		
WY Ant	-1.66	0.50	6150	2.20	3.0	-1.80	-1.82	0.14	106	-1.77	0.14	24
BS Aps	-1.33	0.50	6000	1.80	3.0	-1.50	-1.51	0.11	106	-1.44	0.14	20
XZ Aps	-1.57	0.50	6200	1.90	2.8	-1.60	-1.65	0.15	110	-1.65	0.14	23
DN Aqr	-1.63	0.25	6100	1.80	3.0	-1.70	-1.80	0.15	104	-1.75	0.17	28
DN Aqr	-1.63	0.37	6100	1.80	2.8	-1.70	-1.74	0.13	129	-1.73	0.12	33
SW Aqr	-1.29	0.28	6500	1.90	2.9	-1.40	-1.41	0.15	127	-1.40	0.11	32
SW Aqr	-1.29	0.41	6200	2.00	2.9	-1.40	-1.37	0.20	90	-1.32	0.18	17
X Ari	-2.40	0.19	6650	2.30	2.7	-2.50	-2.54	0.10	35	-2.53	0.21	14
X Ari	-2.40	0.30	6200	1.90	2.8	-2.60	-2.65	0.11	56	-2.66	0.26	20
X Ari	-2.40	0.37	6100	2.15	2.8	-2.60	-2.63	0.10	63	-2.59	0.11	20
X Ari	-2.40	0.47	6000	1.90	2.8	-2.60	-2.57	0.11	72	-2.60	0.14	20
RR Cet	-1.52	0.34	6100	1.70	2.9	-1.50	-1.50	0.13	124	-1.48	0.13	30
RR Cet	-1.52	0.55	5950	1.70	3.1	-1.50	-1.63	0.14	116	-1.63	0.14	32
W Crt	-0.50	0.22	6850	2.00	2.9	-0.50	-0.65	0.14	113	-0.61	0.20	20
W Crt	-0.50	0.32	6650	2.10	2.8	-0.60	-0.58	0.13	111	-0.61	0.14	21
W Crt	-0.50	0.40	6400	2.20	3.0	-0.60	-0.61	0.12	99	-0.59	0.16	19
W Crt	-0.50	0.58	6500	2.60	2.5	-0.50	-0.55	0.21	101	-0.52	0.24	23
DX Del	-0.56	-0.25	6300	2.00	3.2	-0.50	-0.44	0.14	84	-0.47	0.20	15
DX Del	-0.56	0.35	6150	2.00	3.1	-0.60	-0.51	0.15	83	-0.56	0.16	16
DX Del	-0.56	0.42	6150	2.40	3.2	-0.50	-0.31	0.19	68	-0.36	0.28	10
DX Del	-0.56	0.57	6250	2.10	3.4	-0.50	-0.39	0.12	67	-0.46	0.40	13
SX For	-1.62	0.31	6000	1.70	2.7	-1.80	-1.79	0.11	128	-1.79	0.15	33
SX For	-1.62	0.36	6000	1.70	2.8	-1.80	-1.80	0.11	127	-1.79	0.15	33
Sx For	-1.62	0.45	5950	1.70	2.8	-1.80	-1.81	0.12	120	-1.80	0.15	29
DT Hya	...	0.50	6100	2.00	3.1	-1.50	-1.43	0.13	82	-1.35	0.13	18
V Ind	-1.50	0.32	6400	2.00	2.7	-1.50	-1.56	0.10	124	-1.53	0.12	33
V Ind	-1.50	0.40	6200	2.00	2.8	-1.50	-1.67	0.11	128	-1.62	0.19	33
V Ind	-1.50	0.47	6200	2.10	2.7	-1.50	-1.63	0.11	130	-1.62	0.15	32
SSLeo	-1.83	0.31	6200	2.10	2.9	-1.90	-1.87	0.12	113	-1.86	0.15	28
SSLeo	-1.83	0.41	6100	2.10	2.8	-1.80	-1.89	0.14	114	-1.86	0.19	27
SSLeo	-1.83	0.54	6100	2.10	3.0	-1.80	-1.88	0.17	87	-1.82	0.13	22
SSLeo	-1.83	0.56	6000	1.90	2.9	-1.90	-1.93	0.20	92	-1.89	0.14	22
ST Leo	-1.29	0.22	6650	2.00	3.0	-1.30	-1.25	0.21	106	-1.28	0.19	28
ST Leo	-1.29	0.32	6300	1.70	2.7	-1.30	-1.29	0.15	122	-1.26	0.17	30
ST Leo	-1.29	0.45	6150	2.10	2.8	-1.50	-1.41	0.17	130	-1.34	0.24	30
Z Mic	-1.28	0.50	5950	1.60	3.0	-1.40	-1.46	0.12	103	-1.46	0.15	21
RV Oct	-1.34	0.50	6050	1.70	2.8	-1.50	-1.47	0.12	112	-1.44	0.17	22
UV Oct	-1.61	0.50	6050	1.70	2.8	-1.70	-1.69	0.11	115	-1.69	0.12	25
v445 Oph	-0.23	0.28	6600	2.30	2.8	-0.10	0.00	0.17	74	-0.12	0.12	10
v445 Oph	-0.23	0.34	6450	2.40	3.1	-0.10	-0.10	0.17	68	-0.21	0.13	11
v445 Oph	-0.23	0.44	6400	2.40	2.9	-0.10	-0.05	0.12	73	-0.14	0.15	10
v445 Oph	-0.23	0.53	6350	2.60	3.0	-0.10	-0.07	0.16	65	-0.15	0.22	9
AV Peg	-0.14	0.30	6600	2.30	2.8	-0.10	-0.13	0.14	95	-0.17	0.17	17
AV Peg	-0.14	0.36	6500	2.40	2.7	-0.20	-0.15	0.14	88	-0.17	0.16	16
AV Peg	-0.14	0.51	6400	2.60	2.8	-0.20	-0.18	0.19	70	-0.19	0.15	14
AV Peg	-0.14	0.57	6550	2.60	3.1	-0.20	0.02	0.14	67	-0.08	0.19	10

*Table 3 continued on next page*

Table 3 (*continued*)

Star	[Fe/H]	$\phi$	$T_{\text{eff}}$	$\log g$	$\xi_t$	[M/H]	[Fe/H]	$\sigma$	#	[Fe/H]	$\sigma$	#
	Lay94					K	km s <sup>-1</sup>			model		
HH Pup	-0.69	0.13	7050	1.90	3.0	-0.80	-0.80	0.15	96	-0.72	0.15	21
HH Pup	-0.69	0.22	6750	2.00	3.0	-0.80	-0.73	0.10	104	-0.71	0.15	19
HH Pup	-0.69	0.35	6400	2.00	2.7	-0.80	-0.72	0.12	114	-0.72	0.16	23
HH Pup	-0.69	0.45	6250	2.10	2.7	-0.80	-0.73	0.14	112	-0.73	0.17	23
AN Ser	-0.04	0.22	6850	2.10	3.1	0.00	0.05	0.11	77	0.01	0.14	10
AN Ser	-0.04	0.32	6550	2.20	3.0	-0.10	0.08	0.13	70	0.03	0.19	10
AN Ser	-0.04	0.58	6400	2.60	3.1	0.00	0.06	0.15	57	0.04	0.20	12
VY Ser	-1.29	0.23	6200	1.85	2.9	-1.80	-1.92	0.09	105	-1.90	0.14	28
VY Ser	-1.29	0.29	6200	1.85	2.9	-1.80	-1.86	0.10	114	-1.86	0.11	31
VY Ser	-1.29	0.37	6100	1.85	2.8	-1.70	-1.86	0.10	123	-1.86	0.13	31
1645v Sgr	-1.74	0.50	6200	2.00	3.0	-1.80	-1.81	0.13	109	-1.79	0.14	23
W Tuc	-1.64	0.28	6350	1.75	3.0	-1.70	-1.75	0.14	91	-1.73	0.11	27
W Tuc	-1.64	0.40	6100	1.85	3.0	-1.70	-1.77	0.11	114	-1.67	0.17	29
W Tuc	-1.64	0.48	6100	1.85	3.0	-1.70	-1.79	0.13	108	-1.81	0.13	29
CD Vel	...	0.50	6050	1.70	3.0	-1.70	-1.71	0.12	102	-1.73	0.08	22
AS Vir	-1.49	0.50	6000	1.70	2.8	-1.50	-1.59	0.12	108	-1.54	0.15	23
ST Vir	-0.88	0.07	7650	2.00	3.3	-0.90	-0.80	0.16	70	-0.79	0.15	22
ST Vir	-0.88	0.29	6450	1.90	3.1	-0.90	-0.91	0.13	113	-0.89	0.12	20
ST Vir	-0.88	0.51	6300	2.20	2.8	-0.90	-0.85	0.15	100	-0.82	0.19	22
ST Vir	-0.88	0.74	6300	2.20	3.8	-0.90	-0.88	0.15	78	-0.92	0.21	18
ST Vir	-0.88	0.82	6350	2.10	3.7	-0.90	-0.81	0.14	67	-0.89	0.13	13
UU VIr	-0.82	0.25	6450	2.00	2.6	-0.90	-0.97	0.14	114	-0.96	0.19	25
UU Vir	-0.82	0.33	6350	2.00	2.9	-0.90	-0.90	0.10	112	-0.89	0.12	22
UU Vir	-0.82	0.44	6200	1.90	2.7	-0.90	-0.93	0.11	113	-0.92	0.21	25

Table 4. Mean Abundance Ratios

Star	[Fe/H]	[Fe/H]	[Ca/Fe]	[Sc/Fe]	[Ti/Fe]	[Ti/Fe]	[Cr/Fe]	[Cr/Fe]	[Mn/Fe]	[Ba/Fe]
	I	II	I	II	I	II	I	II	I	II
WY Ant	-1.82	-1.77	0.32	0.05	0.39	0.29	0.07	0.03	-0.50	...
BS Aps	-1.51	-1.44	0.28	-0.05	0.27	0.18	0.00	0.07	-0.34	-0.07
XZ Aps	-1.65	-1.65	0.30	0.05	0.32	0.35	0.02	0.10	-0.31	-0.07
DN Aqr	-1.77	-1.74	0.36	0.01	0.34	0.27	0.03	0.11	-0.46	-0.09
SW Aqr	-1.39	-1.36	0.35	-0.17	0.29	0.13	0.02	0.04	-0.35	-0.14
X Ari	-2.60	-2.60	0.35	0.25	0.45	0.44	-0.11	0.21	-0.75	-0.68
RR Cet	-1.57	-1.56	0.31	0.10	0.28	0.24	-0.02	0.07	-0.33	-0.01
W Crt	-0.76	-0.74	0.30	-0.24	0.04	0.03	-0.06	-0.01	-0.26	-0.55
DX Del	-0.52	-0.58	0.07	-0.43	-0.28	-0.11	-0.30	-0.05	0.01	-0.14
SX For	-1.80	-1.79	0.39	-0.02	0.29	0.24	-0.01	0.07	-0.46	-0.13
DT Hya	-1.43	-1.35	0.29	-0.03	0.29	0.27	0.21	0.14	-0.33	...
V Ind	-1.62	-1.59	0.34	-0.02	0.27	0.21	0.05	0.07	-0.43	-0.13
SSLeo	-2.36	-2.32	0.41	0.03	0.48	0.42	0.04	0.29	-0.75	0.05
ST Leo	-1.32	-1.29	0.32	-0.10	0.28	0.23	0.18	0.16	-0.44	-0.03
Z Mic	-1.46	-1.46	0.27	-0.09	0.27	0.25	0.07	0.08	-0.40	-0.06
RV Oct	-1.47	-1.44	0.30	-0.06	0.29	0.21	0.09	0.03	-0.52	-0.32

Table 4 continued on next page

Table 4 (*continued*)

Star	[Fe/H]		[Ca/Fe]		[Sc/Fe]		[Ti/Fe]		[Cr/Fe]		[Mn/Fe]		[Ba/Fe]	
	I	II	I	II	I	II	I	II	I	II	I	II	I	II
UV Oct	-1.69	-1.69	0.29	-0.03	0.25	0.23	0.06	0.10	-0.48	-0.23				
V0445 Oph	-0.05	-0.19	-0.10	-0.58	-0.51	-0.20	-0.15	0.07	0.11	-0.23				
AV Peg	-0.14	-0.20	0.12	-0.43	-0.38	-0.24	-0.23	-0.02	-0.11	-0.30				
HH Pup	-0.95	-0.90	0.06	-0.71	-0.16	-0.27	-0.08	0.02	-0.08	-0.33				
AN Ser	0.06	0.03	0.01	-0.51	-0.46	-0.36	-0.26	-0.01	0.03	-0.32				
VY Ser	-1.88	-1.87	0.35	0.09	0.30	0.28	-0.01	0.08	-0.51	0.02				
v1645 Sgr	-1.81	-1.79	0.31	-0.03	0.31	0.22	-0.06	0.17	-0.34	-0.11				
W Tuc	-1.77	-1.74	0.35	0.02	0.31	0.25	-0.05	0.15	...	0.19				
CD Vel	-1.71	-1.73	0.29	-0.03	0.31	0.25	0.19	0.03	-0.50	-0.09				
AS Vir	-1.59	-1.54	0.31	-0.13	0.26	0.15	0.18	0.10	-0.42	-0.22				
ST Vir	-0.85	-0.86	0.20	-0.24	0.03	0.06	-0.08	0.01	-0.17	-0.31				
UU VIr	-0.93	-0.92	0.23	-0.59	0.10	0.10	0.00	0.09	-0.08	-0.29				
$\langle\sigma\rangle$	0.14	0.16	0.15	0.11	0.11	0.11	0.11	0.13	0.10	0.09				
$\langle\#\rangle$	97	22	8	3	5	7	2	3	2	2				

**Table 5.** Radial velocity and flux measurements.

Star	[Fe/H]	Vamp km s <sup>-1</sup>	DRVm <sup>a</sup> km s <sup>-1</sup>	DRVa <sup>a</sup> km s <sup>-1</sup>	H $\alpha$ flux relative
WY Ant	-1.80	0.83	58.3	116.0	1.20
XZ Aps-1	-1.65	1.10	63.8	124.5	1.25
XZ Aps-2	...	1.10	59.0	...	1.25
DN Aqr	-1.76	0.72	54.0	...	0.44
SW Aqr-1	-1.38	1.28	63.0	120.0	0.38
SW Aqr-2	...	1.28	62.2	...	0.38
X Ari-1	-2.60	0.94	58.8	119.5	1.65
X Ari-2	...	0.94	53.7	...	1.65
RR Cet	-1.57	0.82	59.4	115.5	1.12
W Crt	-0.59	1.10	66.6	111.0	0.07
DX Del	-0.44	0.70	53.3	102.0	0.00
SX For	-1.80	0.64	50.0	101.0	0.18
V Ind	-1.61	1.06	53.5	107.0	0.17
DT Hya	-1.39	0.98	60.7	118.0	0.80
SS Leo-1	-2.34	1.10	60.0	123.0	1.40
SS Leo-2	...	1.10	57.0	...	1.40
ST Leo	-1.31	1.19	64.3	116.0	0.90
Z Mic	-1.46	0.64	51.0	100.5	0.06
RV Oct	-1.46	1.13	63.0	126.0	1.20
V445 Oph	-0.11	0.81	56.0	89.0	0.00
AV Peg	-0.13	0.96	62.0	94.0	0.00
HH Pup	-0.74	1.35	69.7	115.5	0.34
AN Ser-1	+0.05	1.01	59.4	97.0	0.32
AN Ser-2	...	1.01	58.1	...	0.32
VY Ser	-1.88	0.63	49.0	101.0	0.20
W Tuc	-1.74	1.00	61.0	131.0	1.20
CD Vel	-1.72	0.87	51.0	104.0	0.39
ST Vir	-0.86	1.18	56.2	...	0.00
ST Vir	...	1.18	64.0	100.5	0.00
UU Vir-1	-0.93	1.08	68.0	118.0	0.96
UU Vir-2	...	1.08	66.0	...	0.96

<sup>a</sup>typical uncertainties for DRVm are  $\pm 1.5$  km s<sup>-1</sup> and for DRVa are  $\pm 4.0$  km s<sup>-1</sup>

**Table 6.** Rise time, primary & secondary accelerations, radius-variation and  $\gamma$ -velocity.

Star ID	Rise time <sup>a</sup> percent	Primary <sup>a</sup> acceleration km s <sup>-2</sup>	Secondary <sup>a</sup> acceleration km s <sup>-2</sup>	Radius <sup>a</sup> variation R <sub>⊙</sub>	$\gamma$ -velocity <sup>a</sup> km s <sup>-1</sup>
Metal-Poor RR ab stars					
X Ari	13	20.5	2.4	0.90	-38
SS Leo	12	22.6	2.3	0.88	+162
SW Aqr	11	32.5	3.8	0.70	-50
VY Ser	20	14.5	...	0.80	-147
XZ Aps	12	26.1	2.4	0.84	+198
W Tuc	13	22.8	2.9	0.89	+64
DN Aqr	16	18.2	2.8	0.83	-228
SX For	16	16.2	2.4	0.70	+245
WY Ant	14	23.7	3.3	0.79	+204
CD Vel	14	20.4	2.9	0.68	+241
RR Cet	12	24.4	2.8	0.80	-77
V Ind	15	19.1	2.8	0.82	+201
AM Vir	17	18.2	2.9	0.84	+92
RV Oct	11	28.3	3.3	0.79	+141
ST Leo	10	33.3	3.6	0.70	+166
Z Mic	18	17.1	1.3	0.69	-60
DT Hya	12	25.1	2.0	0.79	+80
Metal-Rich RR ab stars					
UU Vir	11	34.6	4.4	0.73	-10
ST Vir	12	31.5	...	0.58	-4
HH Pup	8	45.7	5.0	0.62	+19
DX Del	14	23.4	3.0	0.60	-58
WCrt	9	41.5	4.8	0.61	+61
V445 Oph	13	30.1	...	0.54	-21
AV Peg	14	35.2	4.4	0.57	-60
AN Ser	12	27.5	...	0.69	-43

<sup>a</sup>The error bars are  $\pm 1\%$  for rise time,  $\pm 0.5$  km s<sup>-2</sup> for primary acceleration,  $\pm 1.0$  km s<sup>-2</sup> for secondary acceleration,  $\pm 0.02$  R<sub>⊙</sub> for radius variation, and  $\pm 1.5$  km s<sup>-1</sup> for  $\gamma$ -velocity